Received: 7 November 2023 | Revised: 16 January 2024 | Accepted: 17 January 2024

DOI: 10.1002/alz.13767

Alzheimer's & Dementia®
THE JOURNAL OF THE ALZHEIMER'S ASSOCIATION

RESEARCH ARTICLE

BIN1^{K358R} suppresses glial response to plaques in mouse model of Alzheimer's disease

Laura Fernandez Garcia-Agudo[1] | Zechuan Shi[1] | Ian F. Smith[1] | Enikö A. Kramár[1] | Katelynn Tran[2] | Shimako Kawauchi[2,3] | Shuling Wang[3] | Sherilyn Collins[3] | Amber Walker[3] | Kai-Xuan Shi[3] | Jonathan Neumann[3] | Heidi Yahan Liang[4,5] | Celia Da Cunha[2] | Giedre Milinkeviciute[2] | Samuel Morabito[1] | Emily Miyoshi[1] | Narges Rezaie[4,5] | Angela Gomez-Arboledas[2] | Adrian Mendoza Arvilla[2] | Daryan Iman Ghaemi[1] | Andrea J. Tenner[1,2,6,7] | Frank M. LaFerla[1,2] | Marcelo A. Wood[1,2] | Ali Mortazavi[4,5] | Vivek Swarup[1,2,5] | Grant R. MacGregor[3,4] | Kim N. Green[1,2]

[1]Department of Neurobiology and Behavior, University of California, Irvine, California, USA

[2]Institute for Memory Impairments and Neurological Disorders, University of California, Irvine, California, USA

[3]Transgenic Mouse Facility, ULAR, Office of Research, University of California, Irvine, California, USA

[4]Department of Developmental and Cell Biology, University of California, Irvine, California, USA

[5]Center for Complex Biological Systems, University of California, Irvine, California, USA

[6]Department of Molecular Biology & Biochemistry, University of California, Irvine, California, USA

[7]Department of Pathology and Laboratory Medicine, University of California, Irvine, California, USA

Correspondence
Kim N. Green, Department of Neurobiology and Behavior, University of California, 3208 Biological Sciences III, Irvine, CA, USA.
Email: kngreen@uci.edu

Abstract

INTRODUCTION: The BIN1 coding variant rs138047593 (K358R) is linked to Late-Onset Alzheimer's Disease (LOAD) via targeted exome sequencing.

METHODS: To elucidate the functional consequences of this rare coding variant on brain amyloidosis and neuroinflammation, we generated BIN1^{K358R} knock-in mice using CRISPR/Cas9 technology. These mice were subsequently bred with 5xFAD transgenic mice, which serve as a model for Alzheimer's pathology.

RESULTS: The presence of the BIN1^{K358R} variant leads to increased cerebral amyloid deposition, with a dampened response of astrocytes and oligodendrocytes, but not microglia, at both the cellular and transcriptional levels. This correlates with decreased neurofilament light chain in both plasma and brain tissue. Synaptic densities are significantly increased in both wild-type and 5xFAD backgrounds homozygous for the BIN1^{K358R} variant.

DISCUSSION: The BIN1 K358R variant modulates amyloid pathology in 5xFAD mice, attenuates the astrocytic and oligodendrocytic responses to amyloid plaques, decreases damage markers, and elevates synaptic densities.

KEYWORDS
Alzheimer's disease, astrocytes, BIN1 K358R, inflammation, MODEL-AD, oligodendrocytes

Grant R. MacGregor, Department of Developmental and Cell Biology, University of California, 4213 McGaugh Hall, Irvine, CA, USA.
Email: gmacg@uci.edu

Funding information
National Cancer Institute, Grant/Award Number: P30CA062203; National Institute on Aging, Grant/Award Number: U54 AG054349

Highlights

- *BIN1* rs138047593 (K358R) coding variant is associated with increased risk of LOAD.
- BIN1 K358R variant increases amyloid plaque load in 12-month-old 5xFAD mice.
- BIN1 K358R variant dampens astrocytic and oligodendrocytic response to plaques.
- BIN1 K358R variant decreases neuronal damage in 5xFAD mice.
- BIN1 K358R upregulates synaptic densities and modulates synaptic transmission.

1 | BACKGROUND

Genome-wide association studies (GWAS) established bridging integrator 1 (*BIN1*) as a key risk locus for late-onset Alzheimer's disease (LOAD).[1–3] Subsequent targeted exome sequencing of LOAD patients and controls identified the rare *BIN1* coding variant rs138047593 (K358R) as being associated with increased risk of LOAD.[4,5]

BIN1 (also known as amphiphysin 2) and amphiphysin 1 both function in membrane trafficking and remodeling, including endocytosis.[6] Interestingly, GWAS LOAD studies identified variants associated with other genes whose functions include regulation of endocytosis, including CD2-associated protein (CD2AP), phosphatidylinositol binding clathrin assembly protein (PICALM) and sortilin-related receptor (SORL1).[1,7–9] A body of evidence implicates dysregulation of endocytosis, recycling, and endolysosomal trafficking in the development of LOAD,[10,11] which supports the importance of investigating the effect of coding variants in the endosomal machinery on the development of LOAD-related phenotypes.

BIN1 is transcribed in many different tissues with highest levels in muscle and brain, where it is predominantly expressed in oligodendrocytes and neurons.[12] Alternative splicing produces tissue specific isoforms having different domains (reviewed in[6]). In the brain, BIN1 contains a N-terminal BAR (Bin, Amphiphysin, Rvs[13]) domain that can regulate membrane curvature,[14,15] a central CLAP domain that mediates binding to clathrin and adapter protein 2 (AP2), and a C-terminal SH3 domain that can bind proline-rich-domain-containing proteins, including the AD-associated proteins Tau and clusterin/APOJ.[16–18]

Neuronal BIN1 localizes to the pre-synaptic terminus where it functions in excitatory synaptic transmission via regulation of neurotransmitter vesicle dynamics.[19] BIN1 function has been associated with AD-related pathways. For example, in the absence of BIN1, BACE1 is no longer transported to the lysosome and degraded but instead accumulates in early endosomes, promoting amyloid beta (Aβ) generation.[20–23] BIN1 concentrates around amyloid deposits in AD patients and 5xFAD mice,[24] although a single *Bin1* allele deletion in 5xFAD mice had no overall effect on cerebral amyloid burden.[25] Human studies have found contradictory results when measuring the levels of BIN1 in post-mortem AD brains,[26–30] making it challenging to determine if BIN1 is a critical part of AD pathogenesis.

The BIN1 K358R variant replaces a lysine (K) with an arginine (R) within the RT loop in the SH3 domain,[31] which has the potential to change the way BIN1 interacts with target proteins. An in vitro study reported this variant as a loss of function of BIN1 in the control of Aβ production.[32] Development of mice with a *Bin1*^{K358R} allele would be a powerful resource to evaluate the impact of this coding variant in the development of amyloid and other AD-related pathology.

The Model Organism Development and Evaluation for Late-Onset Alzheimer's Disease (MODEL-AD) program has been introducing LOAD risk variants into the murine genome to help understand how they impact brain biology and aging.[33] Here, we report production and availability of *Bin1*^{K358R} mice and provide phenotyping and transcriptomic data when interbred with the 5xFAD mouse model of amyloidosis. We find that 5xFAD mice homozygous for the *Bin1*^{K358R} allele have altered glial responses to plaques, most notably in astrocytes and oligodendrocytes whose normal responses are impaired/suppressed. This is associated with reduced plasma neurofilament light chain (NfL) in response to plaques, a marker of neuronal damage.

2 | METHODS

2.1 | Animals

All experiments involving mice were approved by the UC Irvine Institutional Animal Care and Use Committee and were conducted in compliance with all relevant ethical regulations for animal testing and research. All experiments involving mice comply with the Animal Research: Reporting In Vivo Experiments (ARRIVE essential 10) guidelines[34] and are provided in the Supplementary Materials.

2.2 | Mice

To generate mice modeling the human BIN1^{K358R} coding variant (B6(SJL)-*Bin1*^{em1Aduci}/J, Jackson Laboratory stock number #035872), Alt-R Crispr RNA (TMF1271 – GATGAGCTGCAACTCAAAGC) and tracrRNA plus CAS9 protein (HiFi Cas9 nuclease V3, Integrated DNA Technologies [IDT], Coralville, IA) as a ribonucleoprotein

(RNP) was microinjected into C57BL/6J zygotes (Jackson Lab Stock # 000664) along with a ssODN sequence (TMF1284–5′-GTTCAAGCCCAGCATGATTACACGGCCACTGACACTGATGAGCTGCAACTGAGGGCTGGCGATGTGGTGTTGGTGATTCCTTTCCAGAACCCAGAGGAG-3′) to introduce the K358R missense variant. G0 founder animals containing the desired DNA sequence changes were backcrossed with C57BL/6J mice and N1 heterozygous mice were sequenced to determine the mutant allele. N1 heterozygous mice were backcrossed to produce N2F1 heterozygotes, which were used to generate animals for subsequent analysis. 5xFAD hemizygous (B6.CgTg[APPSwFlLon,PSEN1*M146L*L286V]6799Vas/Mmjax, Jackson Lab Stock #34848, MMRRC) and non-transgenic littermates were produced by natural mating or in vitro fertilization procedures with C57BL/6J females. After weaning they were housed together with littermates, separated by sex, and aged until the harvest dates. All animals were generated by the Transgenic Mouse Facility at the University of California, Irvine.

2.3 | Genotyping

Oligonucleotides for polymerase chain reaction (PCR)-based genotyping were purchased from IDT. *Bin1*^{K358R} genotyping was performed using a common primer set to amplify both *Bin1* wildtype allele and *Bin1*^{K358R} allele (For 5′-CATGATTACACGGCCACTG-3′ and Rev 5′-TGGGTTCTGGAAAGGAATCAC-3′). Two fluorophore-labeled hydrolysis probes which hybridized specific to mouse *Bin1* wildtype amplicon (5′-CCACATCGCCAGCTTTGAGTTGCAG-3′-HEX) and *Bin1*^{K358R} mutation (5′-CAGCCCTCAGTTGCAGCTCATCAG-3′-FAM) were used to detect the allelic ratio in the amplicon. The relative fluorescence from each probe was quantified at the end point of PCR cycles to call the genotype using the allelic discrimination function of Bio-Rad CFX Maestro software (Bio-Rad, Hercules, CA). For 5xFAD genotyping, a hydrolysis probe which hybridizes to APP(Swe) mutation amplicon was used (For 5′-TGGGTTCAAACAAAGGTGCAA-3′ and Rev 5′-GATGACGATCACTGTCGCTATGAC-3′: APP(Swe) probe 5′-CATTGGACTCATGGTGGGCGGTG-3′) to detect transgenes. We used endogenous *ApoB* allele (For 5′-CACGTGGGCTCCAGCATT-3′ and Rev 5′-TCACCAGTCATTTCTGCCTTTG-3′: *ApoB* probe 5′-CCAATGGTCGGGCACTGCTCAA-3′) to normalize the Ct values.

2.4 | Off-target analysis

Genomic DNA was extracted from mouse tail biopsies using DirectPCR Lysis Reagent (Viagen Biotech, Los Angeles, CA) and Proteinase K (Roche, Indianapolis, IN). Amplification was performed using a Bio-Rad CFX-96 instrument. For each amplicon, a single PCR product was confirmed by capillary electrophoresis (Fragment Analyzer, AATI/Agilent, Santa Clara, CA) then subjected to Sanger sequencing (Retrogen, San Diego, CA) and analyzed using SeqMan Pro 17.2 (DNASTAR, Madison, WI). Primers for PCR amplification and sequencing for off-target analysis are listed in Table S1).

RESEARCH IN CONTEXT

1. **Systematic review**: The authors reviewed the literature using traditional (eg, PubMed) sources, meeting abstracts, and presentations. Results on BIN1 conferring risk for developing LOAD is strong but the mechanisms by which it interacts with aging and pathology to drive AD are unknown. K358R is one of two coding risk variants of BIN1 associated with increased risk of AD and thought to be the more harmful one. Relevant citations are included in the text. By creating mice containing the *BIN1*^{K358R} variant we can explore how these protein sequence changes modulate brain responses to pathology.
2. **Interpretation**: The presence of the *BIN1*^{K358R} variant leads to age-related changes in amyloid beta burden and dampening of astrocytic and oligodendrocytic responses in 5xFAD mice. We provide evidence that the *BIN1*^{K358R} variant regulates numbers of synaptic densities and modulates synaptic plasticity.
3. **Future directions**: The manuscript brings to light significant effects of *BIN1*^{K358R} in 5xFAD mouse model of amyloidosis. Further work is required to evaluate the role of *BIN1*^{K358R} in AD using mouse models that better recapitulate human AD pathology.

2.5 | Histology

Mice were euthanized at 4 and 12 months of age via CO_2 inhalation and transcardially perfused with 1× phosphate buffered saline (PBS). For all studies, brains were removed, and hemispheres separated along the midline. Brain halves were either flash frozen for subsequent biochemical analysis or drop-fixed in 4% paraformaldehyde (PFA; Thermo Fisher Scientific, Waltham, MA) for immunohistochemical analysis. Fixed half brains were sectioned at 40 μm using a Leica SM2000R freezing microtome. All brain hemispheres were processed and coronal brain slices between −2.78 mm posterior and −3.38 mm posterior to Bregma were selected for subsequent analysis.

2.6 | Immunohistochemistry

One representative brain slice from each mouse of the same experimental group (ie, same genotype, age, and sex) was stained in the same well. Free-floating sections were washed three times with 1× PBS for 5 minutes. For Thioflavin-S (Thio-S) staining, a 10-minute incubation in 0.5% Thio-S (1892; Sigma-Aldrich) diluted in 50% ethanol was followed by 2 washes for 5 minutes each in 50% ethanol and one 10-minute wash in 1× PBS. For Amylo-Glo staining, following the PBS washes, free-floating brain slices were washed in 70% ethanol for 5 minutes and rinsed in deionized water for 2 minutes before being

immersed for 10 minutes in Amylo-Glo RTD Amyloid Plaque Staining Reagent (1:100; TR-200-AG; Biosensis, Thebarton, South Australia) diluted in 0.9% saline solution. Afterwards, sections were washed in 0.9% saline solution for 5 minutes and then rinsed in deionized water for 15 seconds before proceeding with a standard indirect immunohistochemical protocol. From the incubation period for both Thio-S and Amylo-Glo onwards, sections were kept protected from light. Sections were immersed in normal blocking serum solution (5% normal goat or donkey serum with 0.2% Triton X-100 in 1× PBS) for 1 hout before overnight incubation at 4°C in primary antibodies diluted in normal blocking serum solution.

Brain sections were stained with primary antibodies against the following: ionized calcium-binding adapter molecule 1 (IBA1; 1:2000; 019-19741; Wako, Osaka, Japan); glial fibrillary acidic protein (GFAP; 1:1000; AB4674; Abcam, Cambridge, MA); S100β (1:200; AB52642; Abcam); lysosome-associated membrane protein 1 (LAMP1; 1:200; AB25245, Abcam); NfL (1:200; AB9568; Sigma-Aldrich); anti-amyloid fibrils OC (OC; 1:1000; AB2286; Sigma-Aldrich); oligodendrocyte transcription factor 2 (OLIG2; 1:500; AB109186, Abcam); SerpinA3N (1:100; AF4709; R&D Systems, Minneapolis, MN); Bassoon (1:250; 75491; Antibodies Inc); and Homer1 (1:250; 160003; Synaptic Systems, Göttingen, Germany).

Whole hemispheres were imaged with a Zeiss Axio Scan Z1 Slide scanner using a 10 × 0.45 NA Plan-Apo objective. High-resolution fluorescence images were obtained using a 20× or 63× objective in a Leica TCS SPE-II confocal microscope and LAS-X software.

2.7 | Synaptic puncta analysis

Brain slices were incubated in blocking buffer (BB; 3% bovine serum albumin [BSA] + 0.2% Triton X-100 in PBS) at room temperature for 1 hour and then incubated overnight at 4°C in BB at 1:250 (3 slices per well) with the pre-synaptic Bassoon (1:250; 75491; Antibodies Incorporated, UC Davis, CA), and post-synaptic Homer1 (1:250; 160003; Synaptic Systems, Göttingen, Germany) antibodies. Slices were then washed three times with wash buffer (WB; 0.2% BSA + 0.05% Triton X-100 in PBS) and incubated at 1:500 in WB at room temperature for 90 minutes with goat anti-mouse IgG CF640R (20304, Biotium, Freemont, CA) and goat anti-rabbit IgG CF568 (Biotium, 20103) antibodies. DAPI was applied to the slices (300 nM) in the final 15 minutes of secondary antibody incubation prior to three washes in WB followed by three washes in PBS. Slices were then adhered to cover glass, allowed to dry, then mounted under 1.5 thickness high-tolerance coverslips using ProLong Glass Antifade Mountant (P36980, Thermo Fisher, Carlsbad, CA). Slices were cured for at least 72 hours prior to imaging.

Super-Resolution imaging was performed using a Zeiss LSM 880 inverted confocal microscope equipped with a Plan-apo 63X/1.4 NA oil objective, in Airyscan mode with a hexagonally packed 32 channel gallium arsenide phosphide photomultiplier tube. Imaging was performed in triplicate per brain region (CA1 or SCX [somatosensory cortex]) with a field of view (FOV) of ≈76 × 76 × 2.16 μm (49 nm pixel size XY, Z-step set to 180 nm).

Airyscan processing of all channels and z-slices was performed in Zen (Zen Blue v3.7, Carl Zeiss, White Plains, NY) using autofilter selected. The processed images were then transferred to Arivis Vision4D 3.1.3 for volumetric reconstruction and analysis. Quantitative comparisons between experimental groups were carried out in sections stained simultaneously with consistent analysis parameters. For synaptic quantification, density of synapses was calculated by determining the number of post- to pre-synaptic puncta occurring within ≤300 nm distance per FOV.

2.8 | Quantification of soluble and insoluble fraction Aβ, NfL, and glial fibrillary acidic protein

Micro-dissected hippocampal and cortical regions of each mouse were flash-frozen and processed for biochemical analysis. Samples were pulverized using a Bessman Tissue Pulverizer. Pulverized hippocampal tissue for biochemical analysis was homogenized in 150 μL of Tissue Protein Extraction Reagent (TPER; Life Technologies, Grand Island, NY), while cortical tissue was homogenized in 1000 μL/150 mg of TPER. This composition of TPER includes 25 mM bicine and 150 mM sodium chloride (pH 7.6) to efficiently solubilize proteins within brain tissue following homogenization. Together with protease (Roche, Indianapolis, IN) and phosphatase inhibitors (Sigma-Aldrich, St. Louis, MO), the homogenized samples were centrifuged at 100,000 × g for 1 hour at 4°C to generate TPER-soluble fractions. For formic acid-fractions, pellets from TPER-soluble fractions were homogenized in 70% formic acid: 75 μL for hippocampal tissue or half of used TPER volume for cortical tissue. Afterwards, samples were centrifuged again at 100,000 × g for 1 hour at 4°C. Protein in the insoluble fraction of micro-dissected hippocampal and cortical tissue was normalized to its respective brain region weight, while protein in soluble fractions was normalized to the protein concentration determined via Bradford Protein Assay. Formic acid neutralization buffer was used to adjust pH prior to running enzyme-linked immunosorbent assays (ELISAs).

Quantitative biochemical analyses of human Aβ soluble and insoluble fraction levels were acquired using the V-PLEX Aβ Peptide Panel 1 (6E10) (K15200G-1; Meso Scale Discovery, Rockville, MD). Quantitative biochemical analysis of NfL in plasma was performed using the R-PLEX Human Neurofilament L Assay (K1517XR-2; Meso Scale Discovery). Quantitative biochemical analysis of soluble glial fibrillary protein (GFAP) fraction level in the cortex of 12-month-old mice was completed using the R-PLEX Human GFAP Assay (K1511MR-2; Meso Scale Discovery).

2.9 | Imaris quantitative analysis

Confocal images of each brain region were analyzed using the spots (for counts) or surfaces (for volumes) modules of Imaris v9.7 and then normalized to the area of the FOV. Quantitative comparisons

between experimental groups were carried out in sections stained simultaneously.

2.10 | Long-term potentiation

Hippocampal slices were prepared from wild-type (WT) and homozygous *BIN1*^{K358R} mice (1 to 2 slice recordings/mouse for 5 mice/genotype totaling $n = 10$ slices/genotype) at 12 months of age. Hippocampal slice preparation and long-term potentiation (LTP) recording was performed as described.[35,36] Following isoflurane anesthesia, mice were decapitated, and the brain was quickly removed and submerged in ice-cold, oxygenated dissection medium containing (in mM) 124 NaCl, 3 KCl, 1.25 KH_2PO_4, 5 $MgSO_4$, 0 $CaCl_2$, 26 $NaHCO_3$, and 10 glucose. Coronal hippocampal slices (340 μm) were prepared using a Leica VT1000S vibrating tissue slicer before being transferred to an Interface recording containing preheated artificial cerebrospinal fluid (aCSF) maintained at 31 ± 1°C and of the following composition (in mM): 124 NaCl, 3 KCl, 1.25 KH_2PO_4, 1.5 MgSO4, 2.5 $CaCl_2$, 26 $NaHCO_3$, and 10 glucose. Slices were continuously perfused with this solution at a rate of 1.75 to 2.00 mL/minute while the surface of the slices were exposed to warm, humidified 95% O_2/5% CO_2. Recordings began following at least 2 hours of incubation. Field excitatory postsynaptic potentials (fEPSPs) were recorded from CA1b striatum radiatum using a single glass pipette filled with 2 M NaCl (2 to 3 MΩ) in response to orthodromic stimulation (twisted nichrome wire, 65 μm diameter) of Schafer collateral-commissural projections in CA1 striatum radiatum (CA1-SR). Following the generation of an input/output curve, the size of the baseline response was established where the current elicited a 50% maximal response. Pulses thereafter were administered at 0.05 Hz. Paired-pulse facilitation was measured at 40, 100, and 200-second intervals prior to setting baseline. After establishing a 20-minute stable baseline, the orthodromic stimulated pathway was used to induce LTP by delivering 5 "theta" bursts, with each burst consisting of four pulses at 100 Hz and the bursts themselves separated by 200 milliseconds (ie, theta burst stimulation [TBS]). The stimulation intensity was not increased during TBS. Data were collected and digitized by NAC 2.0 Neurodata Acquisition System (Theta Burst Corp., Irvine, CA).

2.11 | Bulk RNA sequencing

Frozen tissues were lysed and homogenized using TissueLyser II (Qiagen, Germantown, MD). Total RNAs were extracted using RNeasy Mini Kit (Qiagen) and RNase-Free DNase Set (Qiagen) on a QIAcube (Qiagen) liquid handling platform. RNA integrity number (RIN) was measured by Qubit RNA IQ Assay (Life Technologies) and samples with a RIN of ≥7.0 were kept for complementary DNA (cDNA) synthesis. cDNA synthesis and amplification were performed followed by Smart-seq2 standard protocol.

Libraries were constructed using the DNA Prep Kit (Illumina, San Diego, CA) with an epMotion 5070 TMX (Eppendorf, Enfield, CT) automated pipetting system. Libraries were base-pair selected based on Agilent 2100 Bioanalyzer profiles and normalized by KAPA Library Quantification Kit (Roche). The libraries were built from the hippocampal tissue of 4 to 5 different mice per genotype and sex and sequenced using paired-end 101 bp mode on Illumina NextSeq2000 platform with >28 million reads per sample. Sequences were aligned to the mouse genome (mm10) and annotation was done using GENCODE v21. Reads were mapped with STAR v.2.7.3a and RSEM (v.1.3.3) was used for quantification of gene expression.

2.11.1 | Differential gene expression analysis

Differential gene expression analysis was performed using edgeR per genotype. Genes with a false discovery rate (FDR) of <0.05 were considered differentially expressed. To compare different sets of genes that were differentially expressed we created a binary matrix identifying up- and downregulated genes across different comparisons. Then, lists of genes of interest were chosen to plot a heatmap of their expression and a gene ontology (GO) term enrichment analysis using enrichR (https://amp.pharm.mssm.edu/Enrichr/).

2.12 | Statistics

Every reported n represents the number of independent biological replicates. The sample sizes are similar to those found in prior studies conducted by MODEL-AD.[35] Immunohistochemical and biochemical data and electrophysiology were analyzed using Student's t-test or two-way analysis of variance (ANOVA) with Prism v.9 (GraphPad, La Jolla, CA). Tukey's post hoc tests were utilized to examine biologically relevant interactions from the two-way ANOVA. Student's t-tests were used within genotype groups to study sex differences. Statistical significance was stratified and indicated on the output graphs as $^{*}p \leq 0.05$, $^{**}p \leq 0.01$, $^{***}p \leq 0.001$, $^{****}p \leq 0.0001$. Statistical trends were accepted at $p < 0.10$ ($^{\#}$). Data are presented as standard error of the mean (SEM).

2.13 | Integrated analysis of snRNA-seq data and annotation of cell subpopulations with SPLiT-Seq data from the mouse brain

A unified dataset of gene expression from four different genotypes was constructed using Seurat v4.2.0[37]; an integration framework was also made after eliminating technical artifacts using CellBender v0.2.1.[38] A k-nearest neighbor graph based on the Euclidean distance in principal component analysis space was implemented. We applied the Louvain algorithm to effectively group cells with similar feature expression patterns into local communities and then embedded them with uniform manifold approximation and projection (UMAP). Canonical cell-type markers were used to confirm major cell-type annotations in snRNA-seq cell populations. To define more in-depth subpopulations

of neurons, oligodendrocytes, microglia, astrocytes, and other small cell clusters, we annotated each cell in the snRNA-seq dataset using Seurat label-transfer prediction scores with the snRNA-seq clusters from a published SPLiT-seq dataset of the mouse brain[39] as a reference annotation. Anchor points between the labeled Rosenberg et al. reference dataset and our cortical brain snRNA-seq dataset were identified using the Seurat function FindTransferAnchors. Cell-type prediction scores were computed for all nuclei based on the cell clusters present in the reference dataset. The predicted cell-type annotations were cross-checked with the canonical marker genes for that cluster to give a cell-type annotation for each cluster.

2.14 | snRNA sequencing analysis

2.14.1 | Differential gene expression analysis

Differential gene expression analysis was performed using Seurat MAST in the comparison of 5xFAD hemizygous/*Bin1*^{K358R} homozygous versus 5xFAD hemizygous and *Bin1*^{K358R} homozygous versus WT. Genes with a FDR of <0.05 were considered differentially expressed. To plot different sets of genes differentially expressed, we created an averaged normalized gene expression matrix across all samples within the same genotype group and then plotted identified up- and down-regulated genes across different comparisons. Then, lists of genes of interest were chosen to plot a heatmap of their expression and a GO term enrichment analysis using enrichR (https://amp.pharm.mssm.edu/Enrichr/).

2.14.2 | Annotation of oligodendrocyte subpopulations

snRNA-seq subpopulations for oligodendrocytes were clustered based on the genes that are expressed in at least 5% of cells in our snRNA-seq dataset and in the oligodendrocytes subcluster markers from,[40] as well as other highly variable features identified through FindVariableFeatures. Disease-associated oligodendrocyte (DAO) and homeostatic mature oligodendrocyte lineages were identified along with other mature oligodendrocytes.

2.14.3 | Cellular signaling analysis

Intercellular signaling network analysis was performed using the R package CellChat v1.6.1.[41] Separated CellChat objects were created for all four genotype conditions, grouping by cell classes and using the CellChatDB mouse database for ligand-receptor interactions. The protocol to compare multiple datasets from the CellChat github was followed to process the data. The CellChat function netVisual heatmap was used to view the differential cell communication in each cell class with others between selected genotypes.

2.14.4 | High dimensional weighted correlation gene network analysis

High dimensional weighted gene correlation network analysis (hdWGCNA) was conducted.[42] We filtered by all genes that are expressed in at least 5% of cells to construct the co-expression network and identify modules with minModuleSize = 30. We perform differential module eigengene (DME) analysis between two different genotype groups using the Mann-Whitney *U* test through the function FindDME. Finally, we plotted the GO terms of the selected modules using RunEnrichr, the built-in function of hdWGCNA.

3 | RESULTS

To investigate the effects of the LOAD risk allele *rs138047593*, mice modeling the *BIN1*^{K358R} variant were generated using CRISPR/CAS9 (Figure S1A). The desired sequence change (AAA → AGG; lysine → arginine) and synonymous DNA mutation are shown in Figure S1A. We conducted off-target analyses of other putative cut sites that might have been targeted by CRISPR/CAS9 during generation of the *Bin1*^{K358R} allele. *Bin1*^{K358R} founder mice were backcrossed with WT C57BL/6J animals for three generations before being used to generate animals for this study, making it unlikely that a mutation caused by an off-target effect of CRISPR/CAS9 would be present on a chromosome other than chromosome 18, that is, the location of *Bin1*. Potential CRISPR/CAS9 off-target sites with up to four mismatches using crRNA TMF1271 were screened for using Cas-OFFinder (http://www.rgenome.net/cas-offinder/). Seven potential off-target sites on mouse chromosome 18 were identified (Table S2), five of which were within intronic regions. To screen for evidence of CRISPR/Cas9 RNP activity at each of the five sites, DNA from a WT and two independent homozygous *Bin1*^{K358R} mice were amplified by PCR using the primers listed (Table S1), then sequenced across the potential off-target region at each locus (Figure S1B). None of the five potential off-target sites showed a difference in sequence between WT and homozygous *Bin1*^{K358R} mice. Hereafter, we refer to the *Bin1*^{K358R} allele as BIN1^{K358R}.

3.1 | Changes in fibrillar and non-fibrillar Aβ plaque burden

To explore the interaction between the variant and a relevant AD pathology, we crossed BIN1^{K358R} mice with the 5xFAD mouse model of amyloidosis and assessed the impact on plaque development, as well as the central nervous system (CNS) response to plaques. Hemizygous 5xFAD/homozygous BIN1^{K358R} (hereafter referred to as 5xFAD/BIN1^{K358R}), homozygous BIN1^{K358R} (hereafter referred to as BIN1^{K358R}), hemizygous 5xFAD (hereafter referred to as 5xFAD), and WT control mice were generated and aged until 4 and 12 months,

representing ages defining initial plaque production and advanced plaque load, respectively. All crosses used mice on a co-isogenic or congenic C57BL/6J strain background. We used BIN1^{K358R} homozygotes rather than the heterozygous BIN1^{K358R} allele more commonly found in human individuals to more easily identify phenotypes associated with the K358R variant.

Quantification of staining and immunohistochemistry was performed in the subiculum and visual cortex. The subiculum was chosen due to the high degree of AD-linked pathology present in 5xFAD mice and, concurrently, a more pronounced glial response to that pathology. The subiculum of 4-month-old (4 months) 5xFAD/BIN1^{K358R} mice had fewer and lower total volume of dense-core (ThioS-staining) Aβ plaques compared to 5xFAD controls (Figure 1A,D,E). In the cortex, total plaque volume was significantly reduced in 5xFAD/BIN1^{K358R} mice compared to 5xFAD mice, but plaque density was unchanged (Figure 1A–C). As expected, WT and BIN1^{K358R} mice had no plaques (data not shown). Comparison of the size frequency distribution of average plaque volume in cortex and subiculum (Figure 1J,K) showed relatively more larger plaques present in the visual cortex of 5xFAD (Figure 1J), but not in the subiculum (Figure 1K). At 12 months, ThioS plaque density remained similar between the two genotypes with plaque load in 5xFAD/BIN1^{K358R} mice reaching 5xFAD levels in the cortex (Figure 1A,F,G). In the subiculum, by 12 months of age, ThioS plaque density is comparable between 5xFAD and 5xFAD/BIN1^{K358R} mice (Figure 1A,H), but plaque load is increased in 5xFAD/BIN1^{K358R} mice (Figure 1I). Plaque size frequency evened out between 5xFAD and 5xFAD/BIN1^{K358R} mice in the cortex (Figure 1L) and subiculum (Figure 1M). Diffuse, fibrillar Aβ deposits were quantified by immunofluorescence using the conformation specific antibody OC. At 4 months, there was no difference in OC$^+$ plaque density or total volume between the 5xFAD and 5xFAD/BIN1^{K358R} mice in the cortex (Figure 1N,O). A trend for reduced OC$^+$ plaque density similar to the reduction seen in ThioS density was observed in the subiculum (Figure 1P) of 5xFAD/BIN1^{K358R} mice. However, the OC plaque load was comparable between the two genotypes (Figure 1Q). OC$^+$ plaque density was similar, but plaques were increased in size in the cortex of 12-month 5xFAD/BIN1^{K358R} animals compared to 5xFAD mice (Figure 1R,S). Consistent with increased ThioS plaque load in the subiculum at later ages, 12-month 5xFAD/BIN1^{K358R} animals had increased OC$^+$ plaque number and load (Figure 1T,U). To measure different Aβ species levels directly, micro-dissected cortex and hippocampus from 5xFAD/BIN1^{K358R} and 5xFAD mice were fractionated into detergent soluble and insoluble fractions, and Aβ40 and Aβ42 were quantified (Figure 2). Compared to 5xFAD mice, levels of both Aβ40 and Aβ42 in the soluble fraction of the cortex of 4-month 5xFAD/BIN1^{K358R} mice trended lower (Figure 2A,B), while no differences were seen in the hippocampus (Figure 2C,D). No changes in soluble Aβ40 or Aβ42 levels were detected in either the cortex or hippocampus at 12 months of age (Figure 2E–H). While insoluble levels of both Aβ40 and Aβ42 were comparable between genotypes in the cortex and hippocampus at 4 months of age (Figure 2I–L), at 12 months both were significantly reduced in the cortex (Figure 2 M,N), despite their being higher in plaque and OC total volume. In the hippocampus no change was observed in Aβ40 and Aβ42 levels between 5xFAD and 5xFAD/BIN1^{K358R} mice (Figure 2O,P).

3.2 | Astrocytic response to plaques is impaired in 5xFAD/BIN1^{K358R} mice

We next investigated whether microglial and astrocytic responses to plaques in 5xFAD mice were modulated by the BIN1^{K358R} variant (Figure 3), focusing on the 12-month time point. As expected, the density and average volume of microglia were greater in 5xFAD mice compared to WT controls in both the cortex and subiculum (Figure 3C–F). In contrast, no significant difference was observed between WT and BIN1^{K358R} mice, or between 5xFAD and 5xFAD/BIN1^{K358R} mice in both regions examined (Figure 3A,C–F). Quantification of microglia in contact with ThioS$^+$ dense plaques (Figure 3B) indicated that the number of interactions between microglia and plaques was unchanged between 5xFAD and 5xFAD/BIN1^{K358R} mice.

To explore the astrocytic response to plaques, we performed immunohistochemistry for S100β, a ubiquitous astrocyte marker, and GFAP, a marker constitutively expressed by hippocampal astrocytes, but only expressed by reactive astrocytes in the cortex (Figure 3G). In the cortex, the volume of S100β and GFAP positive cells was increased in 5xFAD mice compared to WT, but were both significantly reduced in 5xFAD/BIN1^{K358R} mice compared to 5xFAD controls (Figure 3H–K), indicating the BIN1^{K358R} variant impaired the astrocytic response to plaques produced by the 5xFAD transgene array. Similarly, a large increase in density of GFAP$^+$ astrocytes induced by plaques in the cortices of 5xFAD animals was reduced in 5xFAD/BIN1^{K358R} mice (Figure 3J). We observed an increased density of GFAP$^+$ astrocytes in the subiculum in both 5xFAD and 5xFAD/BIN1^{K358R} compared to WT mice (Figure 3N), but no difference between the two genotypes. The average volumes of GFAP$^+$ and S100β^+ astrocytes (Figure 3 M,O) as well as the number of S100β^+ astrocytes (Figure 3L) also remained constant between 5xFAD and 5xFAD/BIN1^{K358R} mice. To verify the diminished astrocytic responses observed in the cortex via biochemistry, we quantified GFAP in cortical homogenates and found that GFAP levels were indeed increased in 5xFAD cortices compared to WT mice, but significantly less increased in 5xFAD/BIN1^{K358R} mice (Figure 3P). Together, these results suggest that BIN1^{K358R} is suppressing the normal response by astrocytes to plaques, while not impacting microglia, at least in the cortex.

3.3 | Transcriptomic analyses reveal attenuated glial responses with BIN1^{K358R} variant in 5xFAD mice

To gain a deeper insight into glial changes occurring in 12 months 5xFAD/BIN1^{K358R} mice, we performed bulk-tissue RNA-seq in the hippocampus. Volcano plots revealed no major changes in BIN1^{K358R} versus WT mice (Figure 4A), where only 30 genes were differentially expressed (FDR < 0.05) and none had a significant logFC (>1 or -1). A comparison of 5xFAD versus WT and 5xFAD/BIN1^{K358R}

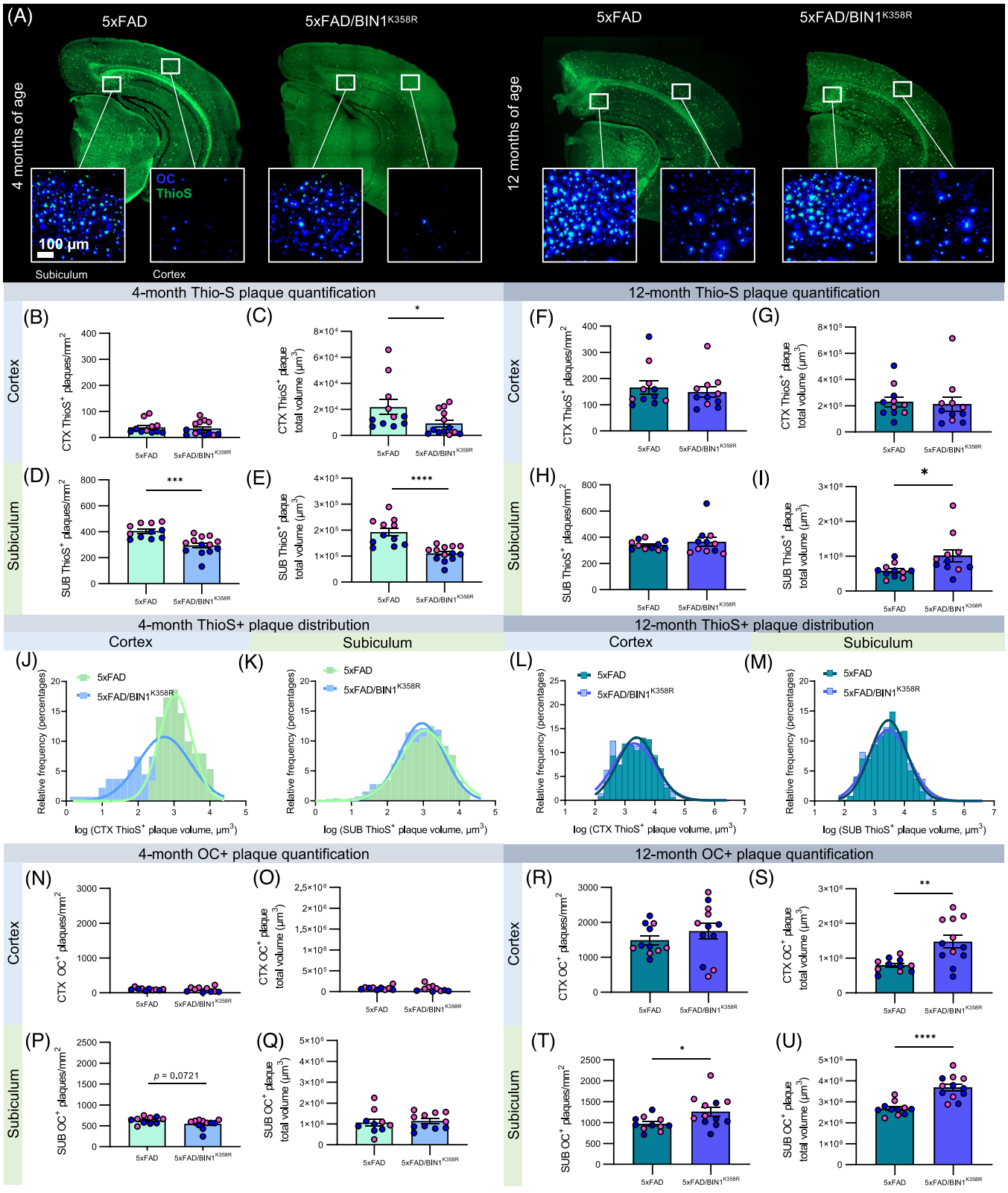

FIGURE 1 Increased amyloid beta plaque burden in 12-month-old (12 months) 5xFAD/*BIN1*^{K358R} mice. (A) Representative brain sections showing whole-brain ThioS^{+} staining in 4-month-old (4 months) and 12 months 5xFAD and 5xFAD/*BIN1*^{K358R} mice. White boxes denote hippocampal subiculum and visual cortex where 20× confocal images were acquired for subsequent analysis. (B,C) ThioS^{+} plaque density and total plaque volume in the visual cortex of 4 months mice. (D,E) ThioS^{+} plaque density and total plaque volume in the subiculum of 4 months mice. (F,G) ThioS^{+} plaque density and total plaque volume in the visual cortex of 12 months mice. (H,I) ThioS^{+} plaque density and total plaque volume in the subiculum of 12 months mice. (J,K) Individual ThioS^{+} plaque size frequency distribution in the visual cortex and subiculum of 4 months mice. (L,M) Individual ThioS^{+} plaque size frequency distribution in the visual cortex and subiculum of 12 months mice. (N,O) OC^{+} plaque density and total

versus 5xFAD mice showed a very similar upregulation (Figure 4B,C) of overall inflammatory genes associated with response to plaque pathology in 5xFAD mice, consistent with previous reports.[35] We next focused our analysis on differences between 5xFAD/BIN1^{K358R} versus 5xFAD mice (Figure 4D), where 263 differentially expressed genes (DEG) were observed. From these DEGs in 5xFAD/BIN1^{K358R} versus 5xFAD mice, 50 are upregulated. Top GO terms for biological processes of the upregulated genes include assembly and organization of neuronal and synaptic structures (Figure 4E, in red), while the top GO hits for the downregulated genes included cell junction disassembly, synapse pruning, and regulation of endosomal transport (Figure 4E, in blue). These GO hits align with the main functions of *Bin1*, which include clathrin-mediated endocytosis, intracellular endosome and vesicle trafficking, cytoskeleton remodeling, and membrane lipid binding to induce membrane curvature.[6,20,32,43] Notably, several of the DEGs in our dataset have been described as marker genes for disease-associated astrocytes (DAAs[44]) and DAOs[45] (Figure 4F). All DAA and DAO genes differentially expressed in our dataset were significantly downregulated in 5xFAD/BIN1^{K358R} versus 5xFAD mice, including *Gfap*, *Vim*, *Aqp4*, *Clu*, *Serpina3n*, *Fxyd1*, *C4b*, and *Cd9*. Furthermore, other pro-inflammatory genes like *Osmr*, *Stat3*, and *Card9* were also downregulated in 5xFAD/BIN1^{K358R} animals. Although the immunohistochemical data showed no difference in astrocytic densities or volumes in the subiculum with either S100β or GFAP, the transcriptional analyses point to an overall suppression of the response of glial cells in the hippocampus to the presence of plaques in 5xFAD/BIN1^{K358R} compared to 5xFAD mice, consistent with the profound suppression of astrocytic responses seen via histology in the cortex.

3.4 | Disease-associated astrocytes and oligodendrocytes are reduced in 5xFAD/BIN1^{K358R} mice

Given the reductions in DAA-associated genes in 5xFAD/BIN1^{K358R} mice, we next explored the impact of the BIN1 variant on DAA and quantified the number of DAA present by combining GFAP and SerpinA3N immunostaining.[44] We found that DAA (GFAP$^+$/SerpinA3N$^+$ cells; Figure 4G) were decreased in the subiculum (Figure 4I), consistent with our hippocampal RNA-seq data. Notably, no change in GFAP$^+$/SerpinA3N$^+$ cells was seen in the cortex, despite a robust reduction in GFAP$^+$ cells (Figure 4H). As expected, very little SerpinA3N$^+$ staining was found in WT mice. As we also found a reduction in DAO-associated genes, we conducted immunostaining for DAO, via antibodies against both OLIG2 and SerpinA3N[45] (Figure 4J). DAO were significantly decreased only in the subiculum of 5xFAD/BIN1^{K358R} mice compared to 5xFAD mice (Figure 4K,L). Interestingly, SerpinA3N was highly upregulated at and around plaques (Figure 4J) of both 5xFAD and 5xFAD/BIN1^{K358R} mice.

Together, these results show that the presence of the BIN1^{K358R} variant alters the glial response to plaques, resulting in a suppression of inflammatory gene expression changes in the hippocampus and a substantially reduced induction of DAA and DAO in the subiculum, despite a slightly elevated plaque load.

3.5 | Single nucleus RNA-seq reveals impairments in cell-cell communication with the BIN1^{K358R} variant

To assess the impact of the BIN1 variant on all CNS cell types in an unbiased manner we performed snRNA-seq on nuclei isolated from the cortex from WT, BIN1^{K358R}, 5xFAD, or 5xFAD/BIN1^{K358R} mice (12 months old; Figure 5A,B). After quality-control filtering, we retained a total of 38,285 nuclei (Figure 5A). We applied UMAP dimensionality reduction and Louvain clustering to the transcriptomic datasets, identifying distinct cell-type clusters in snRNA-seq. Following that, we applied a supervised machine learning approach to predict further the identity of each nucleus based on a well-annotated reference dataset of the mouse brain to resolve transcriptional profiles of many different neuronal, glial, and vascular cell types, specifically region-specific excitatory and inhibitory neurons (Figure 5A and Figure S2).[39]

We observe greatest expression of *Bin1* in oligodendrocytes compared to the rest of the major cell types (Figure 5C), although it is also detected in microglia and inhibitory neurons, as expected. Notably, expression of *Bin1* itself was increased in oligodendrocytes from 5xFAD/BIN1^{K358R} mice versus 5xFAD alone (Figure 5C). To determine how the presence of the BIN1 K358R variant affects gene expression across the major different cell types, we displayed DEG between 5xFAD and 5xFAD/BIN1^{K358R} mice for astrocytes, oligodendrocytes, oligodendrocyte precursors, microglia, excitatory neurons, and inhibitory neurons as a heatmap (Figure 5D). Consistent with our immunohistochemistry data, there is a marked alteration in the response of astrocytes with 5xFAD/BIN1^{K358R}, as well as in oligodendrocytes and oligodendrocyte precursors, compared to 5xFAD mice. Gene expression changes in microglia reveal a unique upregulation of a number of genes in 5xFAD/BIN1^{K358R} compared to 5xFAD mice mainly associated with inflammation, while genes that are upregulated in 5xFAD versus WT mice are not as upregulated in 5xFAD/BIN1^{K358R} mice. Notably, both BIN1^{K358R} and 5xFAD excitatory neurons show similar expression patterns, with 5xFAD/BIN1^{K358R} resembling gene expression in WT neurons. Finally, 5xFAD/BIN1^{K358R} inhibitory neurons show a unique expression pattern compared to the other three genotypes, with many downregulated genes associated with GABA activity. Collectively, these results show that the presence of the

plaque volume in the visual cortex of 4 months mice. (P,Q) OC$^+$ plaque density and plaque total volume in the subiculum of 4 months mice. (R,S) OC$^+$ plaque density and plaque total volume in the visual cortex of 12 months mice. (T,U) OC$^+$ plaque density and plaque total volume in the subiculum of 12 months mice. Data are represented as mean ± SEM. Statistical significance is evaluated by unpaired two-tailed *t*-test; statistical trends are provided as *p*-values on the graphs. $n = 11$ to 13. Pink data points in scatter plots on bar graphs represent female mice, while blue data points represent male mice. CTX, visual cortex; SEM, standard error of the mean; SUB, subiculum. $^*p < 0.05$, $^{**}p < 0.01$, $^{***}p < 0.001$, $^{****}p < 0.0001$.

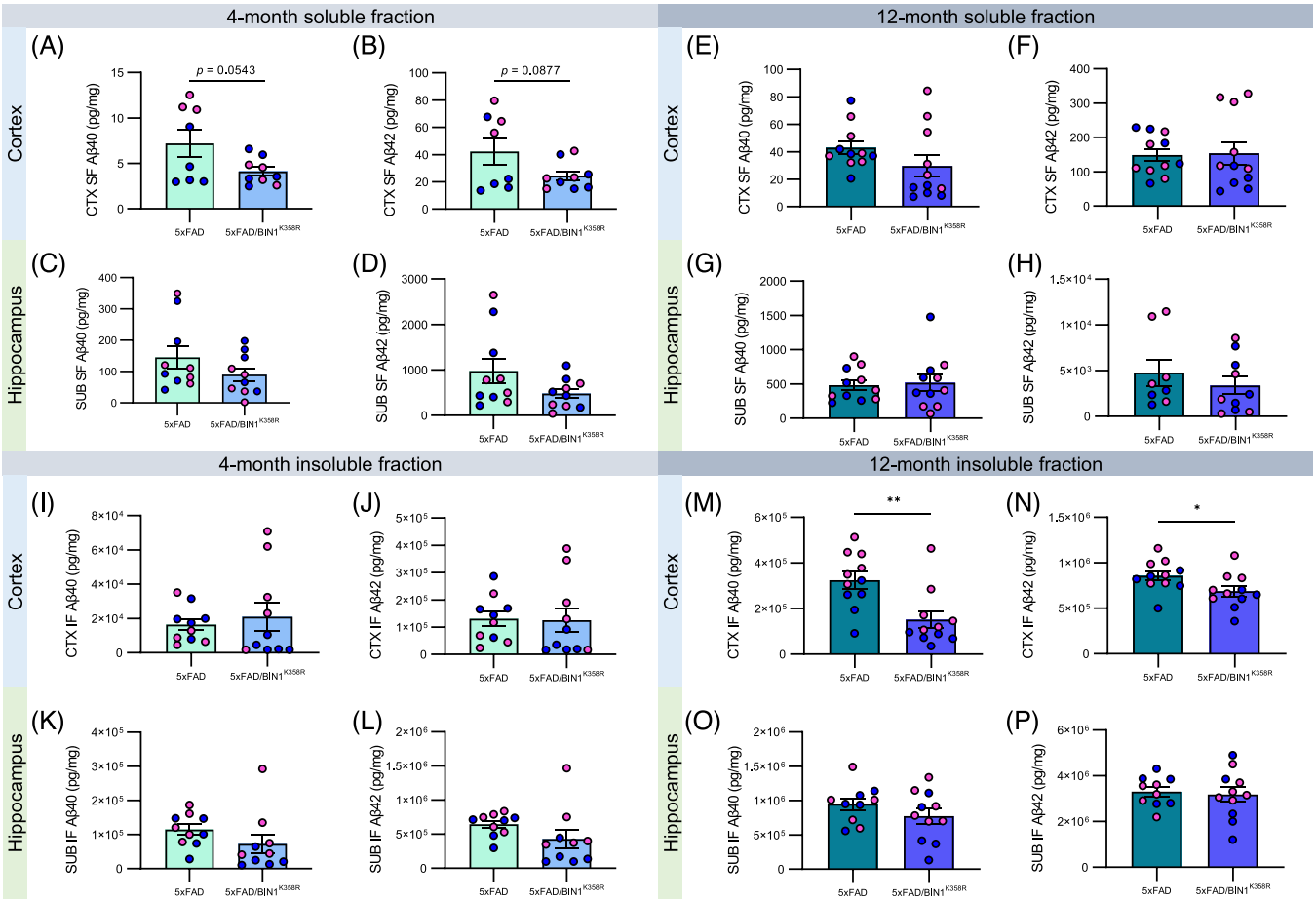

FIGURE 2 Quantification of amyloid beta (Aβ)40-42 in soluble and insoluble fractions from cortex and hippocampus of 5xFAD and 5xFAD/BIN1^{K358R} mice. (A–D) Quantification of Aβ40 and Aβ42 in the soluble fraction of the visual cortex and the hippocampus of 4-month-old (4 months) mice. (E–H) Quantification of the soluble fractions of Aβ40 and Aβ42 in the visual cortex and hippocampus of 12 months mice. (I–L) Quantification of the insoluble fractions of Aβ40 and Aβ42 in the visual cortex and hippocampus of 4 months mice. (M–P) Quantification of the insoluble fractions of Aβ40 and Aβ42 in the visual cortex and hippocampus of 12 months mice. Data are represented as mean ± SEM. Statistical trends are given by *p*-values on the graphs. $n = 8$ to 11. All graphs show an unpaired two-tailed *t*-test. Pink data points in scatter plots with bar graphs represent female mice, and blue data points represent male mice. CTX, visual cortex; IF, insoluble fraction; SF, soluble fraction; SUB, subiculum. $^{*}p < 0.05$, $^{**}p < 0.01$.

5xFAD/BIN1^{K358R} variant has large effects across all major cell types and results in impaired glial responses to plaques.

3.5.1 | Identification of AD-associated oligodendrocytes in 5xFAD/BIN1^{K358R} model with enriched cell-cell interactions

Given the high level of expression of *Bin1* within oligodendrocytes we decided to focus on this cell population and performed status clustering analysis. To explore this population's heterogeneity and disease-associated status, we subclustered the 6192 oligodendrocytes (committed oligodendrocyte precursors [COP], newly formed oligodendrocytes [Oligo NFOL], myelin forming oligodendrocytes [Oligo MFOL], and mature oligodendrocytes [Oligo MOL]; Figure 6A). Oligodendrocyte status clustering from our snRNA-seq data was performed through semi-supervised learning using AD-associated oligodendrocyte markers from[40] (Figure 6A). We discovered an increased ratio of disease-associated oligodendrocyte cluster in both 5xFAD and 5xFAD/BIN1^{K358R} (Figure 6B) compared to WT mice, but no large differences in composition between the 5xFAD and 5xFAD/BIN1^{K358R} cortices. Homeostatic mature oligodendrocytes (homeostatic MOL) were observed in all genotypes, but other transition-like intermediate states of MOL were unable to be further separated. We performed hdWGCNA[42] to further characterize gene expression landscape change within oligodendrocytes among all genotypes (Figure S3A). We found three co-expression modules with comparatively higher scaled expression in DAO: ODC-M2, ODC-M10, and ODC-M17 (Figure S3B). ODC-M2 is significantly downregulated in both BIN1^{K358R} and 5xFAD/BIN1^{K358R} compared to WT and 5xFAD, respectively (Figure 6C,D). For example, hub genes of the DAO-enriched downregulated module ODC-M2 encoded ribonucleoprotein (eg, *Hnrnpht1*,

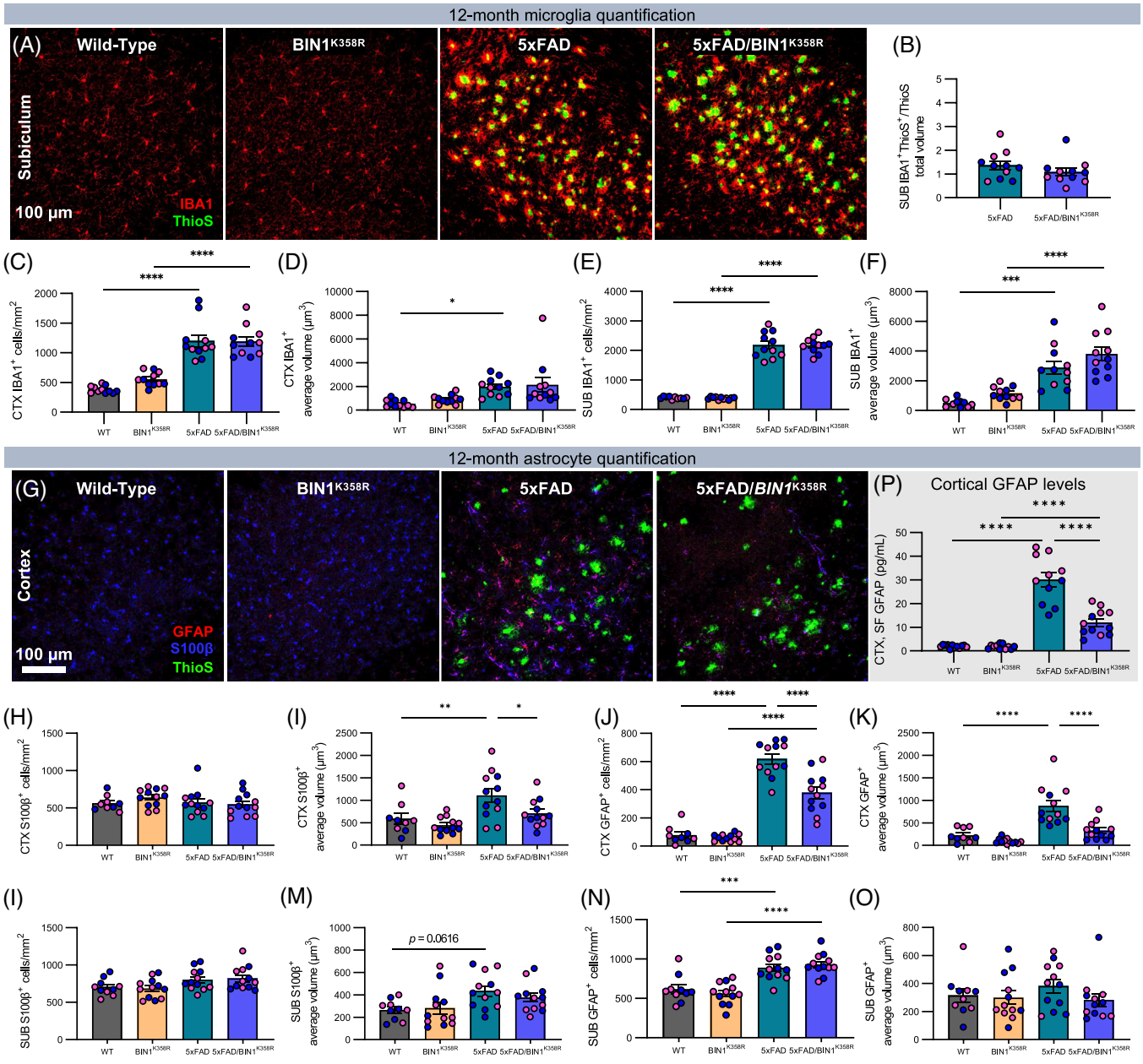

FIGURE 3 Reduced astroglial response in 5xFAD/BIN1^{K358R} mice. (A) Representative images of IBA1 and ThioS stain in the subiculum of 12-month-old (12 months) 5xFAD and 5xFAD/BIN1^{K358R} mice. (B) Quantification of IBA1^{+} microglia in contact with ThioS^{+} plaques (normalized to ThioS^{+} total volume) in the subiculum of 12 months mice. (C,D) IBA1^{+} microglia number and volume in the visual cortex of 12 months mice. (E,F) IBA1^{+} microglia number and volume in the subiculum of 12 months mice. (G) Representative images of GFAP, S100β and ThioS staining in the visual cortex and subiculum of 12 months 5xFAD and 5xFAD/BIN1^{K358R} mice. (H–O) Number and volume of GFAP^{+} and S100β^{+} astrocytes in (H–K) the visual cortex and (L–O) subiculum of 12 months mice. Data are represented as mean ± SEM. $n = 10$ to 13. Statistical trends are given by p-values on the graphs or by # when $0.05 < p < 0.1$ All graphs show a two-way ANOVA with Tukey's multiple comparisons test. Pink data points in scatter plots with bar graphs represent female mice while blue data points represent male mice. CTX, visual cortex; SUB, subiculum. *$p < 0.05$, **$p < 0.01$, ***$p < 0.001$, ****$p < 0.0001$.

Hnrnpu, and *Hnrnpdl*), consistent with its enrichment of GO terms related to diverse cellular processes, including the negative regulation of phosphorylation (Figure S3D and Figure 6E). Additionally, we found more co-expression modules with higher scaled expression in homeostatic MOL, for example, ODC-M1 and ODC-M5 (Figure S3B). Both ODC-M1 and ODC-M5 are significantly downregulated in 5xFAD/BIN1^{K358R} compared to 5xFAD, but not statistically significant in the comparison between BIN1^{K358R} and WT, with its enrichment of GO terms related to axonal transport, phosphatidylinositol 3-kinase activity, cell junction assembly, and adherens junctions (Figure S3E, SF).

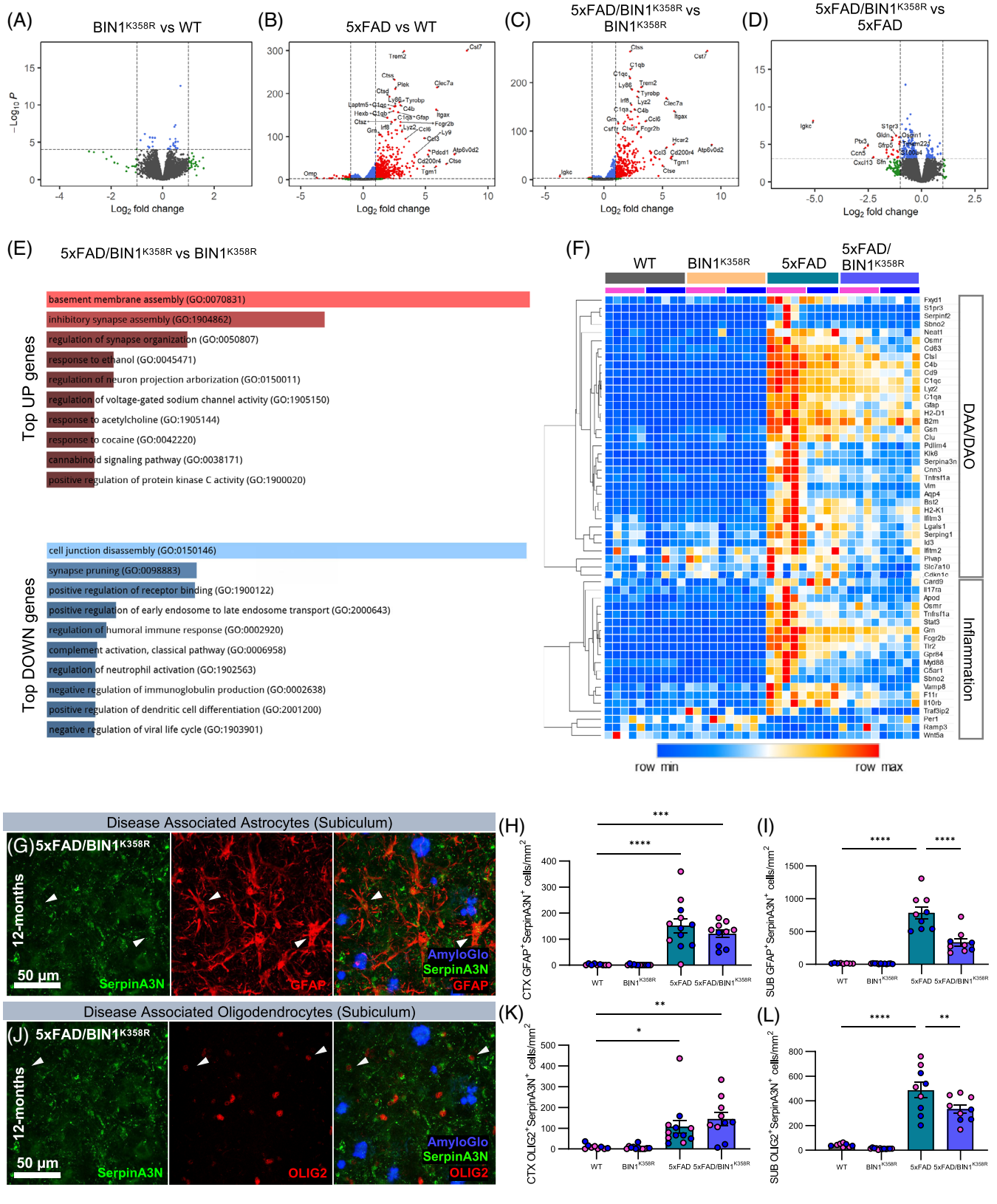

FIGURE 4 Transcriptomic analyses reveal attenuated glial responses upon BIN1^{K358R} in 5xFAD mice. (A–D) Volcano plots showing DEG between 12-month-old (12 months) *BIN1*^{K358R} versus WT mice, 5xFAD versus WT mice, 5xFAD/*BIN1*^{K358R} versus *BIN1*^{K358R} mice, and 5xFAD/*BIN1*^{K358R} versus 5xFAD mice. Blue dots represent significant DEG (FDR < 0.05); red dots represent significant DEG with significant logFC (>1 or <−1); grey and green dots represent non-significant DEG (FDR > 0.05). (E) Top Gene Ontology Biological Process terms obtained in Enrichr for upregulated and downregulated DEG in 5xFAD/*BIN1*^{K358R} versus 5xFAD mice, ranked by combined score. (F) Heatmap of DAA/DAO and inflammation related genes from 5xFAD/*BIN1*^{K358R} versus 5xFAD mice compared across all genotypes. (G) Representative 63× images of

3.5.2 | Cell to cell signaling pathway analyses reveals impeded astrocyte receiver signals in 5xFAD/BIN1^{K358R} mice

Given that astrocytic reaction to plaques is particularly blunted in 5xFAD/BIN1^{K358R} mice, despite minimal expression of *Bin1* within those cells, we explored the potential relative interactions between glial cell types (astrocyte, microglia, DAO, homeostatic MOL, and MOL), and all other cells types using CellChat.[41] The potential differential interactions from signal senders astrocyte, microglia, DAO, homeostatic MOL, and MOL were examined to quantitatively compare the number of interactions and interaction strength with another interacted cell subclass. This analysis revealed a noticeable change in interactions in both number and strength in a cell-cell communication network in BIN1^{K358R} associated genotype groups (BIN1^{K358R} vs WT, Figure 6F; 5xFAD/BIN1^{K358R} vs 5xFAD, Figure 6G). Focusing on 5xFAD/BIN1^{K358R} versus 5xFAD brains, astrocytes were the cell type with the most signaling pathways to other cell types, and with BIN1^{K358R} signaling pathways from astrocytes were increased in both number and strength (Figure 6G). The bar plot at the top of heatmap illustrates the total sum of values in each column, representing incoming signaling and the bar plot on the right represents the total sum of values in each row, indicating outgoing signaling. In terms of color coding inside the heatmap, red indicates an increase in signaling intensity for the WT and 5xFAD when compared to the BIN1^{K358R} and 5xFAD/BIN1^{K358R}; meanwhile, blue represents a decrease in signaling intensity in their respective comparisons. We next looked at cell types that were receiving pathway signals from other cell types (Figure S4A–D). Focusing on astrocytes, we find that the amount of signaling pathways from other cells is reduced in 5xFAD mice compared to WT mice (Figure S4C), and that these pathways are accordingly increased in 5xFAD/BIN1^{K358R} versus 5xFAD brains (Figure S4D). Thus, CellChat analyses show that the presence of plaques tends to decrease signaling pathways to astrocytes from other cell types, and that this decrease is suppressed with the BIN1^{K358R} variant.

3.6 | The impaired glial response to plaques dampens neuronal damage markers with the BIN1^{K358R} variant

Given the profound alterations in astrocyte and oligodendrocyte responses to plaques, we next focused on markers of plaque-induced damage in 12-month-old cohorts of WT, BIN1^{K358R}, 5xFAD, and 5xFAD/BIN1^{K358R} mice. Dystrophic neurites encapsulate dense core plaques and are speculated to contribute to cognitive impairment,[19] and can be visualized with LAMP1 staining. It is established that the microglial response to plaques forms a protective barrier and limits the development of dystrophic neurites.[46–49] Consistent with our observed unchanged number of microglia per plaque, no alterations were seen in the number of LAMP1$^+$ dystrophic neurite halos in the visual cortex (Figure 7A,B) nor in the subiculum of 5xFAD/BIN1^{K358R} mice (Figure 7A–C).

NfL is part of the normal cytoskeleton of healthy brain cells, but upon neuronal injury or disease, including AD, NfL is excessively leaked out of neurons, and eventually reaches the cerebrospinal fluid and the blood, where it also can be measured as a disease or damage biomarker.[50] Plasma NfL increases with disease progression/age in 5xFAD mice, as confirmed here (Figure 7D,E). Quantification of plasma NfL in 5xFAD/BIN1^{K358R} mice revealed no change compared to 5xFAD mice at 4 months but was significantly less than 5xFAD mice at 12 months of age (Figure 7D,E), suggesting that less NfL is released from damaged neurons in the presence of the BIN1^{K358R} variant at this age. Measurements of the soluble and insoluble cortical fractions of NfL at 12 months revealed increases in soluble NfL only in 5xFAD mice, but not 5xFAD/BIN1^{K358R} mice (Figure 7F), while similar elevations in insoluble NfL are found in both 5xFAD and 5xFAD/BIN1^{K358R} mice (Figure 7G). Immunostaining for NfL in brain slices revealed small punctated structures, termed "blebs," localized to the halo of LAMP1$^+$ dystrophic neurites surrounding plaques (Figure 7H), and the quantification of these blebs per FOV showed consistent reductions in 5xFAD/BIN1^{K358R} mice compared to 5xFAD mice at 12 months of age in both the visual cortex and subiculum (Figure 7I,J), in line with the plasma and soluble cortical levels (Figure 7E,F). Thus, despite a slight increase in plaque load, the reduced astrocytic and oligodendrocytic response to plaques appears to result in less NfL release from areas of dystrophic neurites.

3.7 | *BIN1^{K358R}* increases synaptic densities and LTP in the hippocampus

Given the known functions of BIN1 in synaptic vesicle regulation, and studies reporting synaptic deficiencies after BIN1 alterations,[51,52] we quantified pre- and postsynaptic puncta in the CA1 and visual cortex, via super-resolution microscopy, in the 12-month-old cohort. We

SerpinA3N stain in GFAP$^+$ astrocytes in the subiculum of 12 months 5xFAD/*BIN1*^{K358R} mice. (H,I) Quantification of double labeled GFAP$^+$SerpinA3N$^+$ astrocytes in the visual cortex and subiculum of 12 months mice. (J) Representative 63× images of SerpinA3n stain in OLIG2$^+$ oligodendrocytes in the subiculum of 12 months 5xFAD and 5xFAD/*BIN1*^{K358R} mice. (K,L) Quantification of OLIG2$^+$ and SerpinA3N$^+$ oligodendrocytes in the visual cortex and subiculum of 12 months mice. For transcriptomic data statistical significance is delimited by FDR < 0.05; $n = 9$ to 10. Histological data are represented as mean ± SEM; n = 8 to 12. Statistical trends are given by p-values on the graphs or by # when $0.05 < p < 0.1$. Graphs in panels H–L show a two-way ANOVA with Tukey's multiple comparisons test. Pink data points in scatter plots with bar graphs represent female mice while blue data points represent male mice. CTX, visual cortex; DAA, disease-associated astrocytes; DAO, disease-associated oligodendrocytes; DEG, differentially expressed genes; FDR, false discovery rate; SUB, subiculum; WT, wild-type. $^*p < 0.05$, $^{**}p < 0.01$, $^{***}p < 0.001$, $^{****}p < 0.0001$.

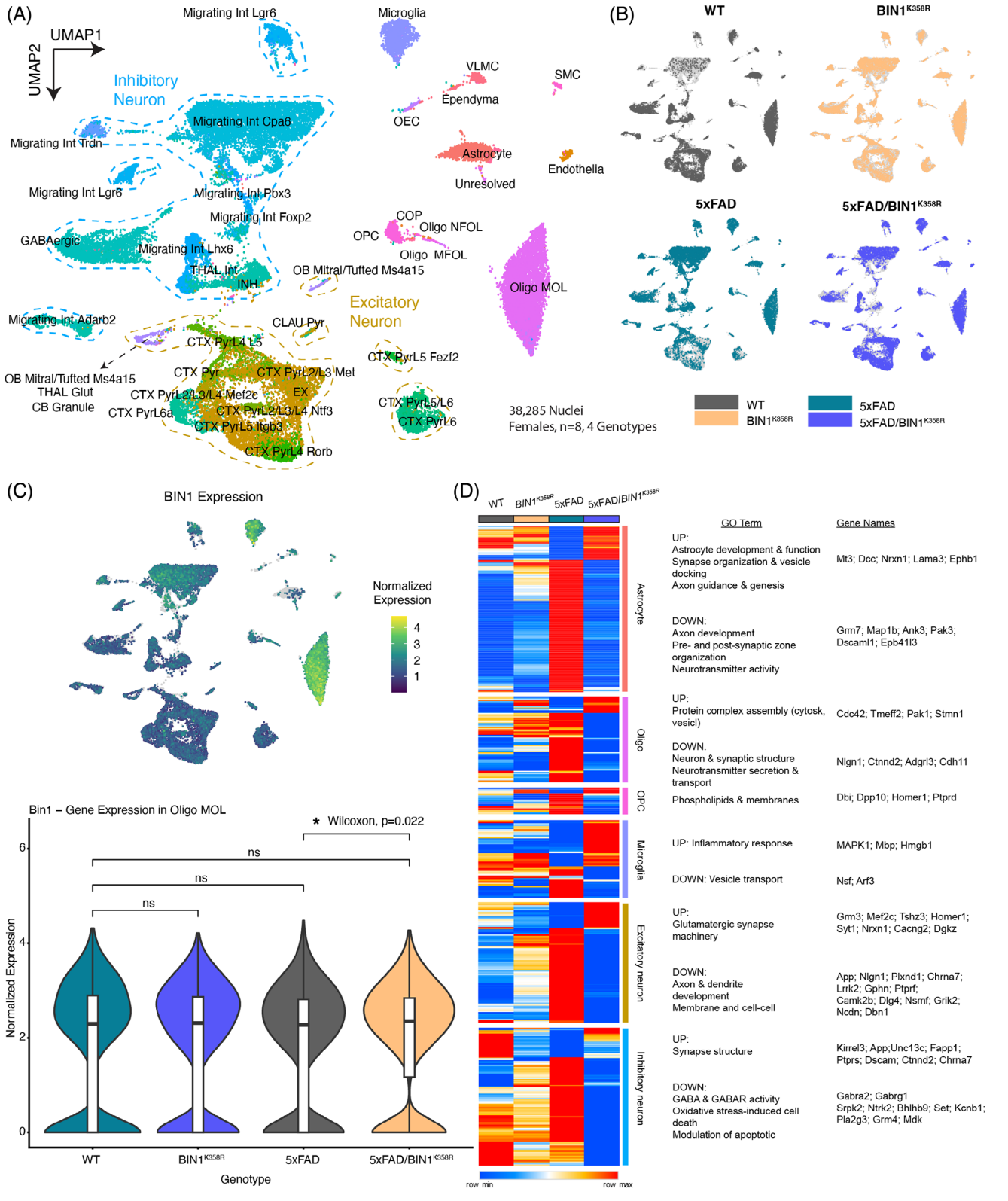

FIGURE 5 snRNA-seq analysis shows BIN1 expression in oligodendrocytes in cortical brain region from mice. (A) Uniform manifold approximation and projection (UMAP) of snRNA-seq analysis of 12-month-old mice provides transcriptomic evidence of 39 distinct clusters, including multiple neuronal subtypes, astrocytes, several oligodendrocyte subtypes, endothelial and other cell clusters. (B) UMAP of snRNA-seq analysis of 12-month-old mice from genotype WT, BIN1^{K358R}, 5xFAD, and 5xFAD/BIN1^{K358R} ($n = 2$). (C) UMAP shows the normalized *Bin1* expression levels. The violin plot presents the normalized *Bin1* expression levels comparison using the Wilcoxon test. (D) Heatmap with gene ontology (GO) term enrichment analysis of differentially expressed gene from 5xFAD/BIN1^{K358R} versus 5xFAD compared across all genotypes. WT, wild-type. ns ($p > 0.05$), $^{*}p < 0.05$.

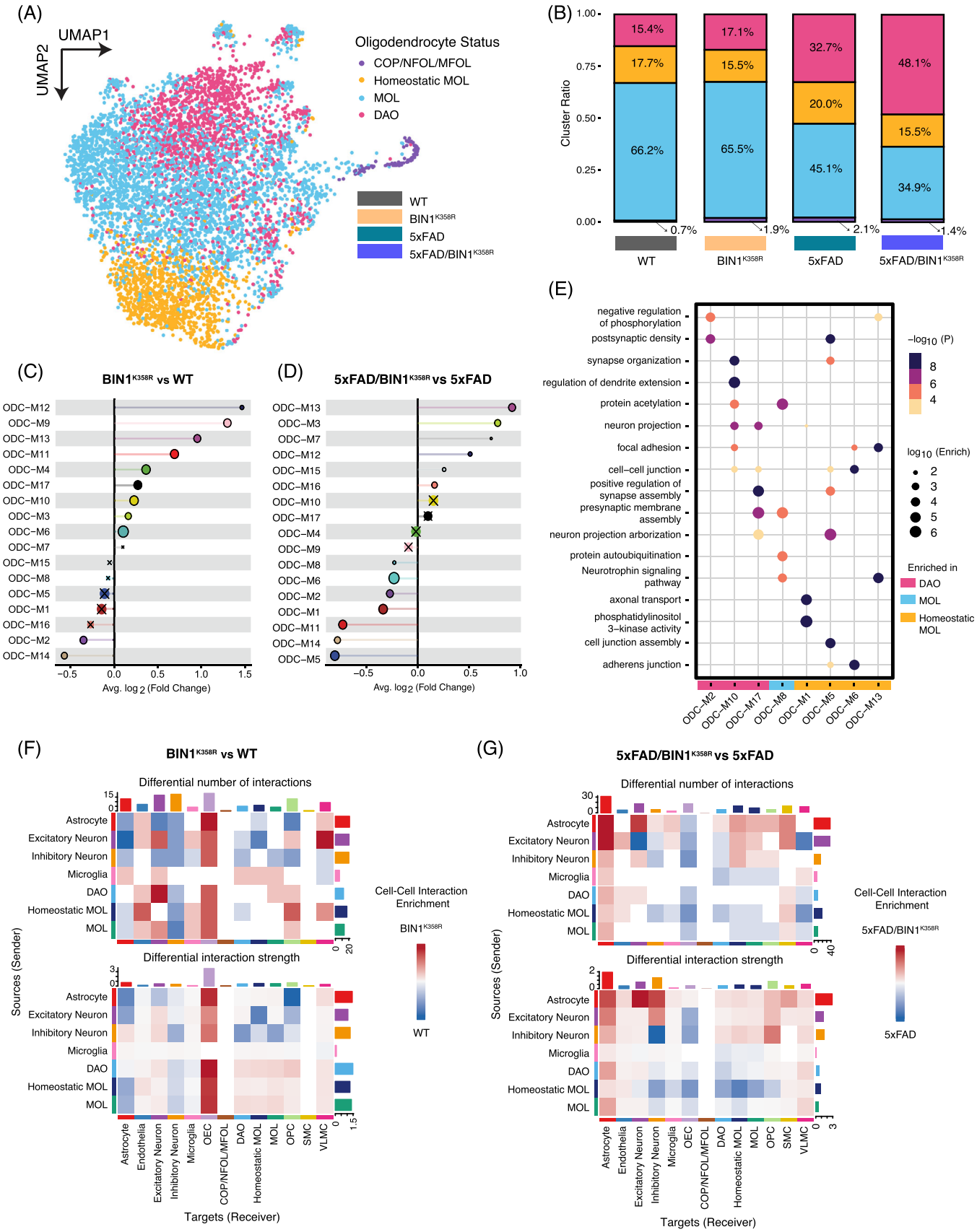

FIGURE 6 snRNA-seq sub-clustering of oligodendrocytes reveals cellular heterogeneity and enriched cell-cell interaction with neurons in 5xFAD/*BIN1K358R* mice. (A) Uniform manifold approximation and projection (UMAP) of oligodendrocyte subclusters. (B) The proportion of oligodendrocyte subclusters by different genotypes. (C) Differential module eigengene (DME) analysis between BIN1K358R and wild-type (WT),

classified pre- and post-synaptic puncta that were within 300 nm of each other as a synapse (Figure 7K). No changes in synaptic densities were observed in the cortex, between any of the genotypes (Figure 7M). In the CA1, synaptic densities were reduced in the 5xFAD and 5xFAD/BIN1^{K358R} mice compared to WT and BIN1^{K358R} mice, respectively. However, the presence of the *BIN1*^{K358R} variant significantly increased synaptic densities in both WT and 5xFAD mice (Figure 7L,N).

To explore functional consequences of increased synaptic densities in the hippocampus we investigated short- and long-term synaptic plasticity in 12-month-old male WT and BIN1^{K358R} mice via pair-pulse facilitation (PPF) and theta burst-induced LTP in acute hippocampal slices. In accordance with the synaptic densities, LTP was enhanced in BIN1^{K358R} compared to WT mice (Figure 7O,P). Basic synaptic transmission was assessed by examining both the input–output curve and paired-pulse facilitation in both groups of mice (Figure 7Q,R). While the input–output curve did not reveal any significant differences in neuronal excitability between groups, there was a significant increase in PPF in BIN1^{K358R} mice compared to their WT controls at each stimulus interval (40, 100, and 200 ms; Figure 7R), strongly suggesting a role for BIN1 as a modulator of presynaptic release.

Taken together, these data show that *BIN1*^{K358R} mutation has a profound impact in synaptic densities in the CA1 region, resulting in functional changes in synaptic transmission.

4 | DISCUSSION

Our results show age-related changes in plaque load and deposition in 5xFAD mice modeling the BIN1^{K358R} variant, with the variant slightly increasing plaque load with age. An altered astrocytic and oligodendrocytic response to these plaques was observed, which correlated with reduced brain and plasma NfL. BIN1^{K358R} also produced an increase in synaptic puncta in the hippocampus. These results support the view that a rare coding sequence variant in the BIN1 gene may affect multiple aspects of AD, and that this new mouse model can be used to interrogate mechanisms of disease pathogenesis.

The *BIN1* locus is associated with the second highest risk for developing LOAD after apolipoprotein E (*APOE*).[1,2,53] Results of studies to determine if variants in *BIN1* are beneficial or harmful to LOAD have been conflicting. In AD, the level of BIN1 has been reported as both increased and decreased.[26–30] BIN1 may regulate the processing of Aβ, but reducing expression of BIN1 in mice did not significantly change Aβ production or deposition.[25] BIN1 has been found to accumulate around amyloid plaques in both humans and mice.[24] BIN1 can directly bind Tau,[17,28] and phosphorylation of Tau in and around the proline-rich domain weakens its interaction with the SH3 domain of BIN1.[17] In a tauopathy model, conditional knockout of neuronal *Bin1* accelerated disease progression, increased Tau deposition and hyperphosphorylation, and caused early death, without increased neuronal loss.[54,55] Partial deletion of BIN1 in tauopathy mice led to worsened disease progression and early death without increased neuronal loss, but also increased Tau deposition and hyperphosphorylation, and reduced Tau spreading in the hippocampus, cortex, and amygdala.[54,56] This illustrates the complex and seemingly conflicting relationship of BIN1 with the pathology of AD.

Two coding variants of BIN1 associated with AD have been discovered in recent years: P318L in Han Chinese individuals[57] and K358R in Caribbean Hispanics.[4] Both BIN1 mutations increased accumulation of Aβ42, reduced control of early endosome size, decreased recycling of BACE1, and reduced interaction with BACE1 in vitro. The K358R mutation was believed to be more harmful than P318L, as re-expression of K358R could not rescue the reduced early endosome size caused by *Bin1* knockdown, and the K358R mutation disrupted BACE1 recycling by a larger extent (70%) compared to the P318L mutation (30%).[32]

To investigate the effect of the BIN1K358R variant in vivo, we introduced the variant into the mouse *Bin1* gene and interbred BIN1 K358R mice with the 5xFAD mouse model of amyloidosis, to explore its impacts on both normal brain function, as well as its interaction with aggressive amyloidosis (ie, induced by the 5xFAD transgene array). The K358R variant is located in the SH3 domain of BIN1, where it binds to proline-rich domains of proteins like Tau, clathrin, and clusterin. The K-R change can alter electrostatic interactions and negatively impact protein folding.[58,59] Notably, the presence of the K358R variant increases plaque load in the subiculum by 12 months of age, mostly through increased plaque size rather than number. Both dense core Thio-S and more diffuse fibrillar plaques (OC$^+$) are affected. This occurs despite a plaque density and size decrease in the subiculum at a younger age of 4 months, which might reflect how the BIN1 K358R variant affects plaque development differently over time. Similar effects of genetic alterations have been reported in amyloidosis mouse models.[60] Notably, we see a slight disconnect between the BIN1 variant-induced increase in plaque load observed and the measurement of total Aβ40 and 42 via biochemistry, where the BIN1 variant decreases total Aβ in the cortex at 12 months of age. Immunohistochemistry measures the total number and size of plaques but cannot readily assess the density of Aβ contained within a plaque, nor the various species of Aβ that may not be detected by either Thio-S stain or the OC antibody. No other BIN1 K358R mouse has been produced or

where in the lollipop plot, the size of each dot corresponds to the number of genes in that module, and "X" is placed over each point that does not reach statistical significance. (D) DME analysis between 5xFAD/BIN1K358R and 5xFAD. (E) Gene ontology (GO) term enrichment analysis of selected differential module eigengene enriched in disease-associated oligodendrocytes (DAO), mature oligodendrocytes (MOL), and homeostatic MOL. (F) Differential number of interactions and interaction strength between BIN1K358R and WT with signal sender from Astrocyte, Excitatory Neuron, Inhibitory Neuron, Microglia, DAO, Homeostatic MOL, and MOL, where red (or blue) color represents increased (or decreased) signaling. (G) Differential number of interactions and interaction strength between 5xFAD/BIN1K358R and 5xFAD with signal sender from Astrocyte, Excitatory Neuron, Inhibitory Neuron, Microglia, DAO, Homeostatic MOL and MOL.

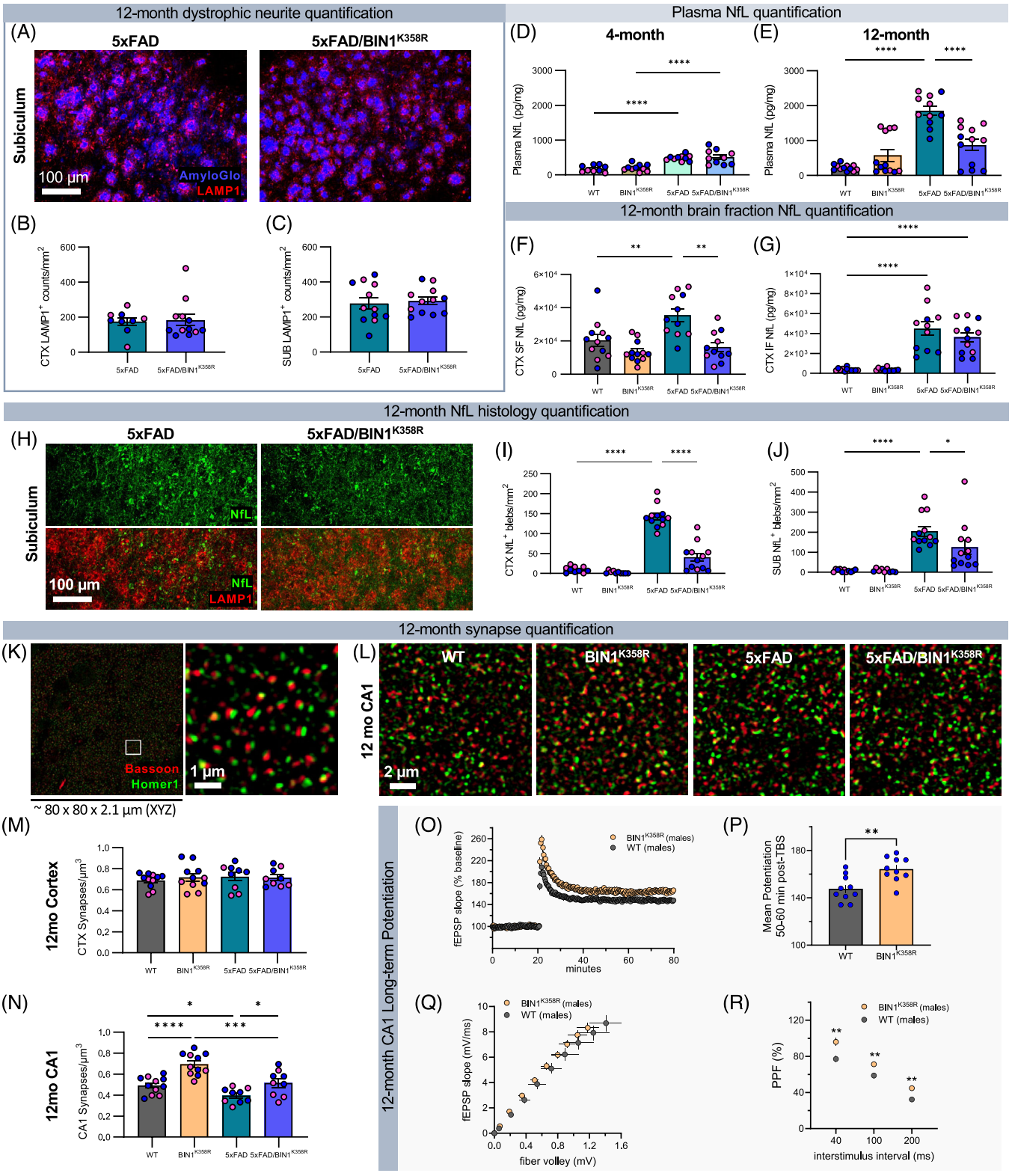

FIGURE 7 Neuronal damage markers are decreased in 5xFAD/BIN1^{K358R} mice. (A) Representative images of LAMP1 and amyloid plaques by Amylo-Glo in the subiculum of 12-month-old (12 months) 5xFAD and 5xFAD/*BIN1*^{K358R} mice. (B–C) Quantification of LAMP1^{+} deposit density and volume ratio to Amylo-Glo^{+} plaques in the visual cortex (B) and subiculum (C) of 12 months mice. (D,E) Plasma neurofilament light chain (NfL) quantification of 4 months (D) and 12 months (E) mice. (F,G) Quantification of soluble (F) and insoluble (G) NfL fractions in the cortex of 12 months mice. (H) Representative images of NfL stain in the subiculum of 12 months 5xFAD and 5xFAD/*BIN1*^{K358R} mice. NfL blebs usually occur in the LAMP1 halo. (I,J) Quantification of brain NfL in the visual cortex (I) and subiculum (J) of 12 months mice. (K) Representative super-resolution image of CA1 immunolabeled with Bassoon for presynaptic elements (red) and Homer1 for postsynaptic elements (green) showing the full captured field of view and a zoomed in box detailing the individual synapses. (L) Representative zoomed in super-resolution images of CA1 from

explored, but a previous report found that K358R mutation resulted in increased accumulation of Aβ42 in vitro.[4,32]

While we observe an appropriate microglial response to these plaques in terms of plaque-associated microglia, we find that the astrocytic response is profoundly blunted. We observe this through impairments in plaque-associated GFAP$^+$ astrocytes in the cortex, both in terms of number and cell size. Direct measurement from cortical lysates also confirms a severely reduced increase in GFAP protein in 5xFAD/BIN1^{K358R} compared to 5xFAD mice. Astrocytes in the hippocampus constitutively express GFAP, and so assessing astrocytic responses to plaques in this brain region is more challenging than in the cortex where astrocytes only express GFAP under reactive conditions. As such we did not observe any changes in S100β or GFAP$^+$ cell densities or sizes in 5xFAD/BIN1^{K358R} mice. However, bulk-tissue RNA-seq from micro-dissected hippocampi also confirmed reduced upregulation of astrocytic genes not only in 5xFAD/BIN1^{K358R} compared to 5xFAD mice, but also in disease-associated oligodendrocyte-related genes. Interestingly, we found that C1qa and C1qc, which both are parts of the C1q protein[61] and primarily produced by microglia in the adult mouse brain,[62] were reduced in the hippocampus of 5xFAD/BIN1^{K358R} compared to 5xFAD mice. C1q, together with TNFα and IL-1α, are secreted by activated microglia and induce neurotoxic reactive astrocytes.[63] This may in part explain why we see diminished reactivity of astrocytes. To further explore changes in glial responses to plaques we took frozen cortical tissue and performed snRNA-seq. We found that the K358R BIN1 variant induces gene expression changes across all major cell types in the brain, but in particular, prevents the stereotypical reaction of astrocytes and oligodendrocytes to the presence of plaques. Given that BIN1 is mostly expressed in oligodendrocytes, and to a lesser extent in microglia and inhibitory neurons, we surmise that the changes in astrocytic response are due to impaired signaling from other BIN1-expressing cells to astrocytes. Indeed, CellChat analyses highlight profound changes in signaling pathways between astrocytes and all other major cell types in the brain.

Given the neuronal expression of BIN1 and that BIN1 functions are at the crossroads of the cellular cytoskeleton and the vesicular system, regulating neurotransmitter vesicle size, maturation, and transport at the synapses, we also investigated synaptic densities. The presence of the BIN1 K358R variant increases synaptic densities in the CA1 in both WT and 5xFAD backgrounds. Notably, there was significant synaptic loss between BIN1^{K358R} and 5xFAD/BIN1^{K358R} mice. We postulate that presence of 5xFAD background drives the synaptic loss; however, since BIN1^{K358R} mice have increased synaptic densities, 5xFAD/BIN1^{K358R} still have more synaptic puncta remaining than 5xFAD mice and, thus, BIN1^{K358R} background may be thought of as exerting a protective effect. Importantly, we were able to explore the functional consequences of synaptic increase in the BIN1^{K358R} cohort of male mice and found presynaptic function was altered with an enhancement in LTP. Previous studies have shown that a lack of brain-specific BIN1 does not affect the number of vesicles per synapse, but causes a decrease of the presynaptic vesicular release and of the recycling vesicle pool size that translates into major learning deficits.[51,64] The observed increase in synaptic densities is potentially consistent with the increase in PPF in BIN1^{K358R} mice due to a greater number of neurotransmitter release sites and/or increased release probability at existing synapses. Also, the concurrent increases in synaptic puncta, PPF, and LTP could point towards a compensatory mechanism of adaptation in the neural circuits of BIN1^{K358R} mice. These changes might be aimed at maintaining synaptic strength or network activity in response to the K358R variant or underlying alterations thereof.

One of the most clinically relevant biomarkers of neuronal injury is the measurement of plasma NfL. We have previously shown that 5xFAD and other mouse models of amyloidosis[35,36] show pathology-dependent increases in plasma NfL that correlate well with plaque load. Here, the presence of the BIN1 K358R variant dramatically reduces plasma NfL despite increased plaque loads, as well as the appearance of NfL blebs in the dystrophic neurites surrounding plaques. These results suggest that the impaired astrocyte and oligodendrocyte responses to the plaques may result in less NfL release from neurons. Interestingly, the microglial response to plaques has been shown to form a protective barrier that restricts the development of surrounding dystrophic neurites, and disruptions in microglial responses to plaques results in increased neuritic damage.[46–49] Here, we observe appropriate microglial accumulation around plaques, and accordingly, no changes in dystrophic neurites are seen as evidenced by LAMP1 quantification. A current topic of debate is whether the microglial response to plaques is ultimately a protective mechanism, restricting plaque growth and dystrophic neurites, or if it results in disease progression through overproduction of inflammatory factors, as well as leading to synaptic and neuronal loss, potentially by facilitating Tau pathology. Thus, it is difficult to evaluate the complete role of the microglial response in animal models that lack the spectrum of pathologies that define human AD—notably mice that recapitulate the spatial and chronological spread of both Aβ and Tau pathologies, and

12-month-old WT, *BIN1*^{K358R}, 5xFAD, and 5xFAD/ *BIN1*^{K358R} mice. (M,N) Quantification of synaptic densities in the cortex (M) and CA1 (N) showing increased synapses with *BIN1*^{K358R} genotype. (O) Time course of field excitatory postsynaptic potential (fEPSP) slope (as percentage of baseline) following theta burst stimulation (TBS, at $t = 20$ min) of slices from 12 months wild-type (WT) and *BIN1*^{K358R} mice showing increased long-term potentiation (LTP) in *BIN1*^{K358R} animals. (P) Mean potentiation (± SEM) during the last 10 minutes of recording in slices from 12 months mice shows increased potentiation in *BIN1*^{K358R} mice ($p = 0.0024$). (Q) Input–output curve over a range of stimulation currents did not reveal any differences between groups (slope of the curves; $p = 0.40$). (R) 12 months *BIN1*^{K358R} mice show increased paired-pulse facilitation (PPF) at all three intervals tested ($F[2,36] = 3.617$, $p = 0.037$). Data are represented as mean ± SEM. $n = 5$ to 6 mice/sex/genotype. LTP: $n = 10$ slices/genotype. Statistical trends are given by p-values on graph. $n = 9$-13. Graphs in panels B and C show an unpaired two-tailed t-test. Graphs in panels D–J, M and N show a two-way ANOVA with Tukey's multiple comparisons test. Pink data points in scatter plots with bar graphs represent female mice, and blue data points represent male mice. CTX, visual cortex; IF, insoluble fraction; SF, soluble fraction; SUB, subiculum. $^*p < 0.05$, $^{**}p < 0.01$, $^{***}p < 0.001$, $^{****}p < 0.0001$.

the downstream effects on the brain, as most studies focus on either a model of amyloidosis (such as this one), or frontotemporal dementia (FTD)-mutation induced tauopathy. Here we find that the BIN1 K358R variant suppresses the appropriate astrocytic and oligodendrocytic response to plaques, seemingly showing protection in the 5xFAD model of amyloidosis. Given the human genetic data, it suggests that the effects of the K358R variant must be deleterious and that we need to identify where and understand how it may be playing a role in disease pathogenesis. As our views on the microglial response to plaques have evolved with emerging data, despite protective effects of anti-inflammatory approaches in models of amyloidosis, our understanding of the response of astrocytes and oligodendrocytes to plaques will also likely evolve. As such, BIN1 will need to be evaluated in more sophisticated models that better recapitulate AD pathology to determine if this impaired/suppressed glial response induced by the K358R variant is protective, or ultimately drives downstream Tau and neurodegeneration.

ACKNOWLEDGMENTS

The authors acknowledge the support of the Chao Family Comprehensive Cancer Center Transgenic Mouse Facility shared resource supported in part by the National Cancer Institute of the National Institutes of Health under award number (P30CA062203) at the University of California, Irvine. This study was supported by the Model Organism Development and Evaluation for Late-Onset Alzheimer's Disease (MODEL-AD) consortium funded by the National Institute on Aging (U54 AG054349).

CONFLICT OF INTEREST STATEMENT

The authors declare that the research was conducted in the absence of any commercial or financial relationships that could be construed as a potential conflict of interest. Author disclosures are available in the supporting information.

CONSENT STATEMENT

No human subjects were used for the present study. Therefore, consent was not necessary.

DATA AVAILABILITY STATEMENT

Protocols, data, and results are available via the AD Knowledge Portal (https://adknowledgeportal.synapse.org). The AD Knowledge Portal is a platform for accessing data, analyses, and tools generated by the Accelerating Medicines Partnership (AMP-AD) Target Discovery Program and other National Institute on Aging (NIA)-supported programs to enable open-science practices and accelerate translational learning. The data, analyses and tools are shared early in the research cycle without a publication embargo on secondary use. Data are available for general research use according to the following requirements for data access and data attribution (https://adknowledgeportal.org/DataAccess/Instructions). Data can be accessed in an interactive matter at UCI Mouse Mind Explorer (admodelexplorer.org).

The Bin1K358R model is available from The Jackson Laboratory (Stock #035872) without restrictions on its use by both academic and commercial users. The content is solely the responsibility of the authors and does not necessarily represent the official view of the National Institutes of Health.

Code used for single-nucleus RNA-seq data integration and label transfer, high dimensional WGCNA, and CellChat analysis are available on a GitHub repository at https://github.com/swaruplabUCI/Phenotyping_Bin1K358R_in_5xFAD_mice_model_2023.

REFERENCES

1. Harold D, Abraham R, Hollingworth P, et al. Genome-wide association study identifies variants at CLU and PICALM associated with Alzheimer's disease. *Nat Genet*. 2009;41:1088-1093.
2. Lambert JC, Ibrahim-Verbaas CA, Harold D, et al. Meta-analysis of 74,046 individuals identifies 11 new susceptibility loci for Alzheimer's disease. *Nat Genet*. 2013;45:1452-1458.
3. Seshadri S, Fitzpatrick AL, Ikram MA, DeStefano AL, Gudnason V, Boada M, et al. Genome-wide analysis of genetic loci associated with Alzheimer disease. *JAMA*. 2010;303:1832-1840.
4. Vardarajan BN, Ghani M, Kahn A, et al. Rare coding mutations identified by sequencing of Alzheimer disease genome-wide association studies loci. *Ann Neurol*. 2015;78:487-498.
5. Luukkainen L, Helisalmi S, Kytovuori L, et al. Mutation analysis of the genes linked to early onset Alzheimer's disease and frontotemporal lobar degeneration. *J Alzheimers Dis*. 2019;69:775-782.
6. Prokic I, Cowling BS, Laporte J. Amphiphysin 2 (BIN1) in physiology and diseases. *J Mol Med*. 2014;92:453-463.
7. Hollingworth P, Harold D, Sims R, et al. Common variants at ABCA7, MS4A6A/MS4A4E, EPHA1, CD33 and CD2AP are associated with Alzheimer's disease. *Nat Genet*. 2011;43:429-435.
8. Naj AC, Jun G, Beecham GW, et al. Common variants at MS4A4/MS4A6E, CD2AP, CD33 and EPHA1 are associated with late-onset Alzheimer's disease. *Nat Genet*. 2011;43:436-441.
9. Rogaeva E, Meng Y, Lee JH, et al. The neuronal sortilin-related receptor SORL1 is genetically associated with Alzheimer disease. *Nat Genet*. 2007;39:168-177.
10. Szabo MP, Mishra S, Knupp A, Young JE. The role of Alzheimer's disease risk genes in endolysosomal pathways. *Neurobiol Dis*. 2022;162:105576.
11. Van Acker ZP, Bretou M, Annaert W. Endo-lysosomal dysregulations and late-onset Alzheimer's disease: impact of genetic risk factors. *Mol Neurodegener*. 2019;14:20.
12. Butler MH, David C, Ochoa G-C, et al. Amphiphysin II (SH3P9; BIN1), a member of the amphiphysin/Rvs family, is concentrated in the cortical cytomatrix of axon initial segments and nodes of Ranvier in brain and around T tubules in skeletal muscle. *J Cell Biol*. 1997;137:1355-1367.
13. Simunovic M, Evergren E, Callan-Jones A, Bassereau P. Curving cells inside and out: roles of BAR domain proteins in membrane shaping and its cellular implications. *Annu Rev Cell Dev Biol*. 2019;35:111-129.
14. Ren G, Vajjhala P, Lee JS, Winsor B, Munn AL. The BAR domain proteins: molding membranes in fission, fusion, and phagy. *Microbiol Mol Biol Rev*. 2006;70:37-120.
15. Meunier B, Quaranta M, Daviet L, Hatzoglou A, Leprince C. The membrane-tubulating potential of amphiphysin 2/BIN1 is dependent on the microtubule-binding cytoplasmic linker protein 170 (CLIP-170). *Eur J Cell Biol*. 2009;88:91-102.
16. Cousin MA, Robinson PJ. The dephosphins: dephosphorylation by calcineurin triggers synaptic vesicle endocytosis. *Trends Neurosci*. 2001;24:659-665.
17. Sottejeau Y, Bretteville A, Cantrelle FX, et al. Tau phosphorylation regulates the interaction between BIN1's SH3 domain and Tau's proline-rich domain. *Acta Neuropathol Commun*. 2015;3:58.
18. Zhou Y, Hayashi I, Wong J, Tugusheva K, Renger JJ, Zerbinatti C. Intracellular clusterin interacts with brain isoforms of the bridg-

ing integrator 1 and with the microtubule-associated protein Tau in Alzheimer's disease. *PLoS One*. 2014;9:e103187.
19. Kandalepas PC, Sadleir KR, Eimer WA, Zhao J, Nicholson DA, Vassar R. The Alzheimer's beta-secretase BACE1 localizes to normal presynaptic terminals and to dystrophic presynaptic terminals surrounding amyloid plaques. *Acta Neuropathol*. 2013;126:329-352.
20. Miyagawa T, Ebinuma I, Morohashi Y, et al. BIN1 regulates BACE1 intracellular trafficking and amyloid-beta production. *Hum Mol Genet*. 2016;25:2948-2958.
21. Leprince C, Le Scolan E, Meunier B, et al. Sorting nexin 4 and amphiphysin 2, a new partnership between endocytosis and intracellular trafficking. *J Cell Sci*. 2003;116:1937-1948.
22. Ubelmann F, Burrinha T, Salavessa L, Gomes R, Ferreira C, Moreno N, et al. Bin1 and CD2AP polarise the endocytic generation of beta-amyloid. *EMBO Rep*. 2017;18:102-122.
23. Lambert E, Saha O, Soares Landeira B, et al. The Alzheimer susceptibility gene BIN1 induces isoform-dependent neurotoxicity through early endosome defects. *Acta Neuropathol Commun*. 2022;10:4.
24. De Rossi P, Andrew RJ, Musial TF, et al. Aberrant accrual of BIN1 near Alzheimer's disease amyloid deposits in transgenic models. *Brain Pathol*. 2019;29:485-501.
25. Andrew RJ, De Rossi P, Nguyen P, et al. Reduction of the expression of the late-onset Alzheimer's disease (AD) risk-factor BIN1 does not affect amyloid pathology in an AD mouse model. *J Biol Chem*. 2019;294:4477-4487.
26. Glennon EB, Whitehouse IJ, Miners JS, et al. BIN1 is decreased in sporadic but not familial Alzheimer's disease or in aging. *PLoS One*. 2013;8:e78806.
27. Glennon EB, Lau DH, Gabriele RMC, et al. Bridging Integrator-1 protein loss in Alzheimer's disease promotes synaptic tau accumulation and disrupts tau release. *Brain Commun*. 2020;2(1):fcaa011.
28. Chapuis J, Hansmannel F, Gistelinck M, et al. Increased expression of BIN1 mediates Alzheimer genetic risk by modulating tau pathology. *Mol Psychiatry*. 2013;18:1225-1234.
29. Karch CM, Jeng AT, Nowotny P, Cady J, Cruchaga C, Goate AM. Expression of novel Alzheimer's disease risk genes in control and Alzheimer's disease brains. *PLoS One*. 2012;7:e50976.
30. Marques-Coelho D, Iohan L, Melo de Farias AR, et al. Differential transcript usage unravels gene expression alterations in Alzheimer's disease human brains. *NPJ Aging Mech Dis*. 2021;7:2.
31. Owen DJ, Wigge P, Vallis Y, Moore JD, Evans PR, McMahon HT. Crystal structure of the amphiphysin-2 SH3 domain and its role in the prevention of dynamin ring formation. *EMBO J*. 1998;17:5273-5285.
32. Perdigao C, Barata MA, Burrinha T, Guimas Almeida C. Alzheimer's disease BIN1 coding variants increase intracellular Abeta levels by interfering with BACE1 recycling. *J Biol Chem*. 2021;297:101056.
33. Oblak AL, Forner S, Territo PR, et al. Model organism development and evaluation for late-onset Alzheimer's disease: MODEL-AD. *Alzheimers Dement*. 2020;6:e12110.
34. Percie du Sert N, Ahluwalia A, Alam S, et al. Reporting animal research: explanation and elaboration for the ARRIVE guidelines 2.0. *PLoS Biol*. 2020;18:e3000411.
35. Forner S, Kawauchi S, Balderrama-Gutierrez G, et al. Systematic phenotyping and characterization of the 5xFAD mouse model of Alzheimer's disease. *Sci Data*. 2021;8:270.
36. Javonillo DI, Tran KM, Phan J, et al. Systematic phenotyping and characterization of the 3xTg-AD mouse model of Alzheimer's disease. *Front Neurosci*. 2021;15:785276.
37. Hao Y, Hao S, Andersen-Nissen E, et al. Integrated analysis of multimodal single-cell data. *Cell*. 2021;184:3573-3587. .e29.
38. Stephen JF, Mark DC, Alessandro A, et al. Unsupervised removal of systematic background noise from droplet-based single-cell experiments using CellBender. *Nat Methods*. 2022;20(9):1323-1335.
39. Rosenberg AB, Roco CM, Muscat RA, et al. Single-cell profiling of the developing mouse brain and spinal cord with split-pool barcoding. *Science*. 2018;360:176-182.
40. Park H, Cho B, Kim H, et al. Single-cell RNA-sequencing identifies disease-associated oligodendrocytes in male APP NL-G-F and 5XFAD mice. *Nat Commun*. 2023;14(1):802.
41. Jin S, Guerrero-Juarez CF, Zhang L, et al. Inference and analysis of cell-cell communication using CellChat. *Nat Commun*. 2021;12:1088.
42. Morabito S, Reese F, Rahimzadeh N, Miyoshi E, Swarup V. hdWGCNA identifies co-expression networks in high-dimensional transcriptomics data. *Cell Rep Methods*. 2023;3:100498.
43. Tan MS, Yu JT, Tan L. Bridging integrator 1 (BIN1): form, function, and Alzheimer's disease. *Trends Mol Med*. 2013;19:594-603.
44. Habib N, McCabe C, Medina S, et al. Disease-associated astrocytes in Alzheimer's disease and aging. *Nat Neurosci*. 2020;23:701-716.
45. Kenigsbuch M, Bost P, Halevi S, et al. A shared disease-associated oligodendrocyte signature among multiple CNS pathologies. *Nat Neurosci*. 2022;25:876-886.
46. Wang HF, Wan Y, Hao XK, et al. Bridging integrator 1 (BIN1) genotypes mediate Alzheimer's Disease risk by altering neuronal degeneration. *J Alzheimers Dis*. 2016;52:179-190.
47. Condello C, Yuan P, Schain A, Grutzendler J. Microglia constitute a barrier that prevents neurotoxic protofibrillar Abeta42 hotspots around plaques. *Nat Commun*. 2015;6:6176.
48. Condello C, Yuan P, Grutzendler J. Microglia-mediated neuroprotection, TREM2, and Alzheimer's disease: evidence from optical imaging. *Biol Psychiatry*. 2018;83:377-387.
49. Yuan P, Condello C, Keene CD, et al. TREM2 haplodeficiency in mice and humans impairs the microglia barrier function leading to decreased amyloid compaction and severe axonal dystrophy. *Neuron*. 2016;90:724-739.
50. Bacioglu M, Maia LF, Preische O, et al. Neurofilament light chain in blood and CSF as marker of disease progression in mouse models and in neurodegenerative diseases. *Neuron*. 2016;91:56-66.
51. De Rossi P, Nomura T, Andrew RJ, et al. Neuronal BIN1 regulates presynaptic neurotransmitter release and memory consolidation. *Cell Rep*. 2020;30:3520-3535. .e7.
52. Schurmann B, Bermingham DP, Kopeikina KJ, et al. A novel role for the late-onset Alzheimer's disease (LOAD)-associated protein Bin1 in regulating postsynaptic trafficking and glutamatergic signaling. *Mol Psychiatry*. 2020;25:2000-2016.
53. Seshadri S, Fitzpatrick AL, Ikram MA, et al. Genome-wide analysis of genetic loci associated with Alzheimer disease. *JAMA*. 2010;303:1832-1840.
54. McAvoy KM, Rajamohamed Sait H, Marsh G, et al. Cell-autonomous and non-cell autonomous effects of neuronal BIN1 loss in vivo. *PLoS One*. 2019;14:e0220125.
55. Ponnusamy M, Wang S, Yuksel M, et al. Loss of forebrain BIN1 attenuates hippocampal pathology and neuroinflammation in a tauopathy model. *Brain*. 2022;146(4):1561-1579.
56. Ponnusamy M, Wang S, Yuksel M, et al. Loss of forebrain BIN1 attenuates hippocampal pathology and neuroinflammation in a tauopathy model. *Brain*. 2023;146:1561-1579.
57. Tan MS, Yu JT, Jiang T, Zhu XC, Guan HS, Tan L. Genetic variation in BIN1 gene and Alzheimer's disease risk in Han Chinese individuals. *Neurobiol Aging*. 2014;35:1781.e1-1781.e8.
58. Sokalingam S, Raghunathan G, Soundrarajan N, Lee SG. A study on the effect of surface lysine to arginine mutagenesis on protein stability and structure using green fluorescent protein. *PLoS One*. 2012;7:e40410.
59. Tiller KE, Li L, Kumar S, MC Julian, Garde S, Tessier PM. Arginine mutations in antibody complementarity-determining regions display context-dependent affinity/specificity trade-offs. *J Biol Chem*. 2017;292:16638-16652.

60. Jay TR, Hirsch AM, Broihier ML, et al. Disease progression-dependent effects of TREM2 deficiency in a mouse model of Alzheimer's disease. *J Neurosci*. 2017;37:637-647.
61. Chen G, Tan CS, Teh BK, Lu J. Molecular mechanisms for synchronized transcription of three complement C1q subunit genes in dendritic cells and macrophages. *J Biol Chem*. 2011;286:34941-34950.
62. Fonseca MI, Chu SH, Hernandez MX, et al. Cell-specific deletion of C1qa identifies microglia as the dominant source of C1q in mouse brain. *J Neuroinflammation*. 2017;14:48.
63. Liddelow SA, Guttenplan KA, Clarke LE, et al. Neurotoxic reactive astrocytes are induced by activated microglia. *Nature*. 2017;541:481-487.
64. Di Paolo G, Sankaranarayanan S, Wenk MR, et al. Decreased synaptic vesicle recycling efficiency and cognitive deficits in amphiphysin 1 knockout mice. *Neuron*. 2002;33:789-804.

SUPPORTING INFORMATION

Additional supporting information can be found online in the Supporting Information section at the end of this article.

How to cite this article: Garcia-Agudo LF, Shi Z, Smith IF, et al. BIN1^{K358R} suppresses glial response to plaques in mouse model of Alzheimer's disease. *Alzheimer's Dement*. 2024;20:2922–2942. https://doi.org/10.1002/alz.13767